J. Plasma Phys. (2026), *vol.* 92, E49 © The Author(s), 2026. Published by Cambridge University Press. This is an Open Access article, distributed under the terms of the Creative Commons Attribution-NonCommercial-NoDerivatives licence (https://creativecommons.org/licenses/by-nc-nd/4.0/), which permits non-commercial re-use, distribution, and reproduction in any medium, provided that no alterations are made and the original article is properly cited. The written permission of Cambridge University Press or the rights holder(s) must be obtained prior to any commercial use and/or adaptation of the article.

doi:10.1017/S0022377826101421

ARC physics basis–magnetohydrodynamics†

N. Leuthold[1], N.C. Logan[1], D.A. Burgess[1], A.O. Nelson[1], S. Benjamin[2], C. Hansen[1], A. Kumar[2], C.F.B. Zimmermann[1], F. Carpanese[3], A.J. Creely[4], J.C. Hillesheim[4], M. Muraca[2] and C. Paz-Soldan[1]

[1]Columbia University, New York, NY, USA
[2]Massachusetts Institute of Technology, Cambridge, MA, USA
[3]Neural Concept, Lausanne 1015, Switzerland
[4]Commonwealth Fusion Systems, Cambridge, MA, USA

Corresponding author: N. Leuthold, nils.leuthold@columbia.edu

(Received 18 October 2025; revision received 23 December 2025; accepted 30 January 2026)

ARC is designed to produce 400 MW of net electricity and prove the commercial feasibility of a fusion power plant. In order to achieve this goal ARC has to operate with optimal core performance in a stationary scenario that minimises wear on the first wall and divertor. This requires avoiding or mitigating magnetohydrodynamic (MHD) instabilities which have the potential to not only degrade the plasma core but also lead to deleterious transient heat loads on plasma facing components. Therefore, this work aims at characterising the MHD stability of the high performance ARC scenario and inform the design of error field correction coils. Firstly, simulations of vertical displacement events show that an in-vessel coil is not needed and instead the poloidal shaping coils can be used to control vertical stability. These simulations also inform the demands on the corresponding coil power supplies. Stability analysis of the ideal kink mode with or without a conducting wall and kinetic effects suggests that the ARC baseline scenario operates deeply in the stable region. Using RDCON, tearing modes at the $m/n = 2/1$ and $3/2$ surfaces (with poloidal mode number m, and toroidal mode number n) are shown to be linearly stable, and including thermal transport effects in the rational surfaces lead to further stabilisation. However, other transient plasma instabilities can seed neoclassical tearing modes (NTMs). The marginally stable width of NTMs in ARC strongly depends on the internal inductance and can fall below 0.1 % of the normalised poloidal flux. Furthermore, an empirical cross-machine model of the $n = 1$ error field leading to a disruption predicts a critical error field larger than SPARC but smaller than ITER. Three-dimensional coils can be designed with the Generalised Purturbed Equilbium Code based on a simple model that calculates the maximum correctable error field that is limited by the neoclassical toroidal viscosity torque. Broad scans of different coil geometries identify a set of 2 rows of off-midplane coils to be a suitable solution. It is also determined that such a set of three-dimensional coils is capable of correcting $n = 2$ error fields to some degree and creating strong enough $n = 2$ or $n = 3$ edge resonant perturbation fields

†This article has been updated since original publication. A notice detailing the change has been published (DOI: 10.1017/S0022377826101822).

for the suppression of edge-localised modes at reasonable coil currents. The final design of the first ARC will be further informed by results from SPARC.

Key words: fusion plasma, plasma instabilities

1. Motivation

The ARC™[1] tokamak, designed to be a commercial fusion power plant (FPP), is part of a class of future machines that will operate as commercial power plants rather than flexible experimental devices. The manifestation of fusion-relevant plasmas at this scale will require robust operation to minimise the risk from plasma instabilities and disruptions, with more stringent limitations on diagnostics and control than on present research devices. For this reason, stable plasma scenarios must be designed and assessed prior to machine operation.

In this paper, we discuss scenario and machine optimisation in ARC through the lens of magnetohydrodynamic (MHD) stability and control. In tokamaks, MHD stability can manifest itself through various critical phenomena, including the triggering of deleterious edge-Localised modes (ELMs) or global modes like the $n = 0$ and $n = 1$ modes, where n is the toroidal mode number of the instability. These instabilities place both hard and soft limits on the achievable plasma pressure normalised by the magnetic field pressure, known as the plasma beta (β), and constrain the operational space available to any given machine.

In order to assess the role that MHD stability will play in defining the accessible scenarios on the ARC tokamak, we utilise a series of well-validated physics codes to understand how changes in the ARC machine design will impact performance and control of the baseline power-producing scenario. As the design of ARC is still evolving, the following analyses are based on the ARC Version 3A and directly inform future iterations.

In § 2 the kinetic profiles and equilibrium as well as predicted rotation profiles used throughout this study are introduced. The first MHD stability investigated is the vertical stability control in § 3. Next, in § 4 the intrinsic three-dimensional (3-D) stability of the ARC baseline scenario is predicted. Specifically the ideal kink beta limit, linear tearing stability and neoclassical tearing modes are assessed. Lastly, in § 5 the critical $n = 1$ error field causing locked modes and disruptions is predicted, and a physics basis to inform the design of error field correction coils (EFCCs) is formulated.

2. The ARC kinetic equilibrium and profiles

For an as accurate as possible analysis of MHD physics a kinetic equilibrium is required in addition to estimated rotation profiles. This section describes how the kinetic profiles, rotation profiles and the kinetic equilibrium were informed and calculated. The starting point for this is a magnetic equilibrium generated by FreeGS (Dudson 2024) that was identified with cfsPOPCON (Body 2025) to meet the ARC target of approximately 400 MW of net electricity with a fusion gain factor of $Q = 50$. ARC uses an up–down symmetric double-null configuration with a triangularity of about 0.65 and elongation of 1.8. More information on the process to generate this magnetic equilibrium is provided in Hillesheim *et al*. (2026).

[1]SPARC® and ARC™ are trademarks of Commonwealth Fusion Systems®.

https://doi.org/10.1017/S0022377826101421 Published online by Cambridge University Press

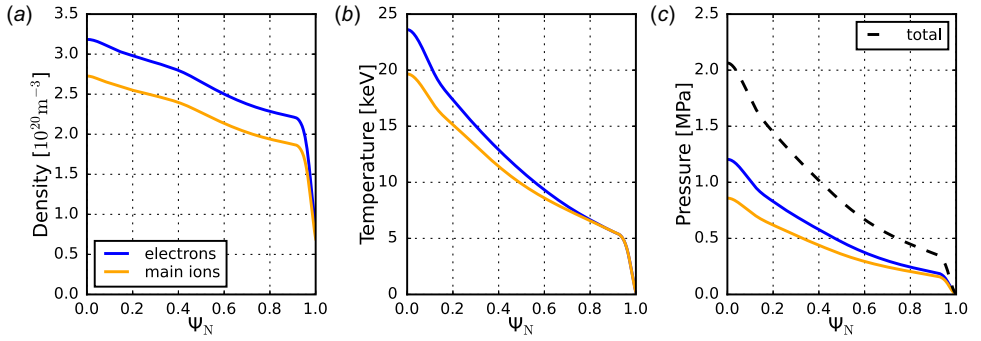


FIGURE 1. Radial profiles of the electron and ion density (*a*), temperature (*b*) and pressure (*c*) as a function of the normalised poloidal flux. The dashed pressure line indicates the total pressure.

2.1. *Kinetic profiles*

The kinetic profiles are based on a combination of EPED (Snyder *et al*. 2009, 2011) to set the H-mode pedestal width and height, and turbulent transport simulations to calculate the profiles in the core region. The core profiles used here are informed by ASTRA (Pereverzev & Yushmanov 1991) coupled to the transport model TGLF (Staebler, Kinsey & Waltz 2004) using saturation rule SAT2 (Staebler *et al*. 2020). Furthermore, the separatrix temperature and density are informed by compatibility with detachment and operation in an ELM-free regime (Eich *et al*. 2026). An overview of the transport simulation informing the ARC kinetic profiles as well as further high-fidelity simulations of core transport can be found in Howard *et al*. (2026).

The profiles of electron and main ion densities, temperatures and pressures are shown in figure 1 after slight smoothing and adding a boundary condition on the magnetic axis of vanishing derivatives. The main ions (50/50 deuterium and tritium) contribute to 85 % of the electron density across the entire radial range. The remaining electrons are the result of helium ash, hydrogen for ion cyclotron minority heating, tungsten and additional heavier impurities injected into the plasma to achieve the desired effective charge Z_{eff}. They are not further specified at this stage and a constant Z_{eff} of 1.5 is assumed across the entire plasma.

2.2. *Kinetic equilibrium*

The recently developed Grad–Shafranov solver TokaMaker (Hansen *et al*. 2024) is used to calculate the Grad–Shafranov equilibrium which can be seen in figure 2(*a*). In order to reproduce the shape of the original FreeGS magnetic equilibrium the TokaMaker calculation is constrained by the two main *x*-points as well as a list of isoflux points that span the last closed flux surface (LCFS) of the original magnetic equilibrium all the way into the closed divertor. The high-field side (HFS) and low-field side (LFS) gaps between the wall and LCFS are set to approximately 2 cm. The kinetic profiles discussed in the previous section are used to constrain the pressure (*b*) and current profiles (*c*) including the bootstrap current j_{BS} (Sauter, Angioni & Lin-Liu 1999) over the whole radial range. ARC is designed to have a right-hand helicity with a negative plasma current I_{p} and negative toroidal magnetic field B_{T} pointing in the same toroidal direction. This results in a positive safety factor q profile, as seen in figure 2(*b*) with $q_0 < 1$ and $q_{95} = 3.77$. Rational surfaces used in

https://doi.org/10.1017/S0022377826101421 Published online by Cambridge University Press

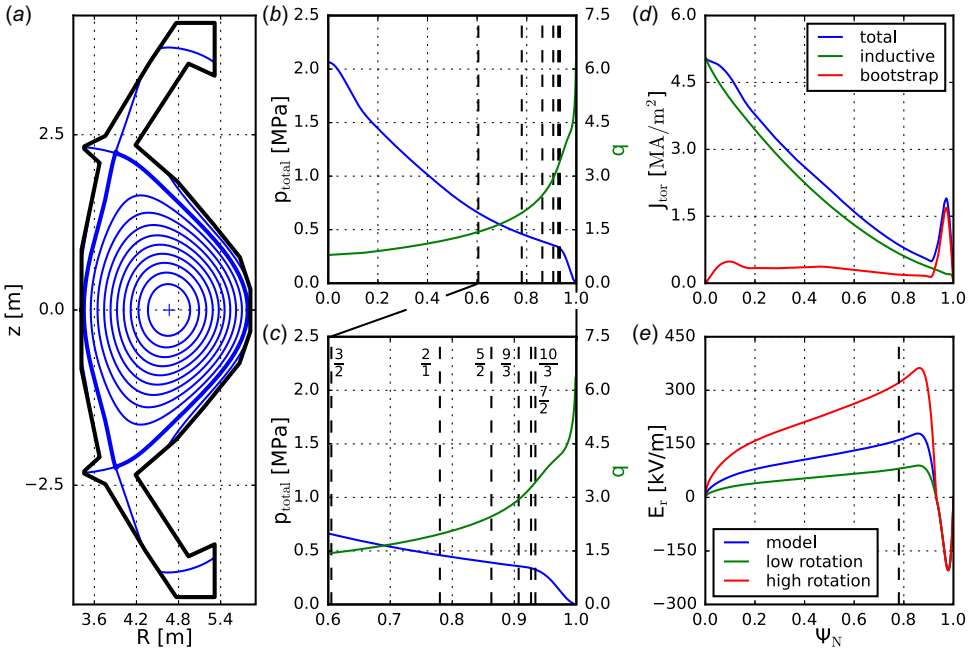


FIGURE 2. (*a*) Poloidal cross-section of the kinetic equilibrium. (*b*) Total pressure and safety factor profile with relevant core and pedestal top rational surfaces indicated by vertical dashed lines with zoom-in in (*c*). (*d*) Current profiles and (*e*) radial electric field profiles from empirical extrapolations (blue) and a low rotation (green) and high rotation (red) case assuming a variation of 0.5× and 2.0× of the model results to cover the uncertainty bands. The vertical dashed line in (*e*) indicates the $q = 2$ surface location which the empirical model was developed for.

the following studies are marked in figure 2(*b*) with vertical dashed lines in the core at $q = 1.5, 2.0, 2.5$ and in the edge near the pedestal top at $q = 3.0, 3.33, 3.5$.

2.3. *Rotation estimates*

Because the workflows used in § 5 depend strongly on the $\boldsymbol{E} \times \boldsymbol{B}$ rotation with the electric field $\boldsymbol{E}$ and the magnetic field $\boldsymbol{B}$, predictions are made in the following to derive an $\boldsymbol{E} \times \boldsymbol{B}$ rotation profile for ARC. Since ARC will use purely wave heating and no neutral beam injection, no substantial external torque input can be provided. Although substantial progress has been made over the last years in understanding the intrinsic torque and intrinsic plasma rotation, scalings and extrapolations are still uncertain and many contradicting scalings can be found (Rice *et al*. 2007; Grierson *et al*. 2013; Chrystal *et al*. 2020). Hence, the following extrapolations should be viewed with scepticism and we try to address this issue by including low and a high rotation cases to evaluate the impact of the highly uncertain rotation prediction.

In order to estimate a radial electric field and consequent $\boldsymbol{E} \times \boldsymbol{B}$ rotation, we split the radial electric field E_r profile up into a core and an edge part separated by a zero crossing assumed to be at a normalized poloidal flux of $\Psi_N = 0.93$ which is close to the pedestal top. Furthermore we assume a vanishing radial electric field at the separatrix. In the core, the radial electric field is defined mostly by the contribution from the toroidal rotation, which is estimated based on an empirical scaling developed in Rice *et al*. (2007) for purely wave-heated plasmas including multiple tokamaks of varying size. In particular, the toroidal rotation measured on the $q = 2$

https://doi.org/10.1017/S0022377826101421 Published online by Cambridge University Press

surface normalised to the Alfvén velocity, that is the Alfvén Mach number M_A, was identified to scale well with the toroidal beta β_t and the cylindrical safety factor q^* as $M_A = 0.65\beta_T^{1.4}q^{*2.3}$. While this scaling was only developed for the rotation at the $q = 2$ surface, the codes used in this work require complete radial profiles. Therefore it is assumed that it is a reasonable approximation in the whole core region ranging from $\Psi_N = 0.0$ to $\Psi_{q=2} + 0.05$. In the edge, the radial electric field in an H-mode plasma typically forms a so-called E_r well. Due to the steep gradients at this location, for the main ions species the diamagnetic term in the radial ion force balance is dominant and can be used as an approximation for the E_r well (Viezzer *et al*. 2013). Combining the E_r estimates in the core and edge results in the radial electric field profiles as shown in figure 2(*e*) for the three different cases: the model prediction (blue), a high rotation case with 2x the intrinsic rotation prediction (red) and a low rotation case with a multiplier of 0.5 (green). This captures the uncertainty of the model well.

Furthermore, a simple model for error field correction introduced later in Appendix A requires the intrinsic torque of the plasma. The intrinsic torque for ARC V0 is also predicted in Rice *et al*. (2021) as $T_0 = 8$ Nm. Considering the uncertainties in this model and the current ARC V3A design, using the scaling law a reasonable intrinsic torque would be in the range of 5–20 Nm.

Currently, rotation modelling lacks a precise boundary condition in the plasma edge, as the underlying physical processes are still under discussion. Therefore, to map out the effects of various models, a second workflow is applied using an alternative approach. Within the plasma core, turbulent momentum transport governs the formation of the rotation profile in the absence of strong transient events. Under these conditions, the workflow presented in Zimmermann *et al*. (2024), which incorporates semi-empirical and validated turbulent momentum transport models, can be applied. For this purpose, it is conservative to assume zero edge rotation, for example, at the pedestal top. A dimensionless, normalised version of this model yields an intrinsic torque of approximately 30 Nm at the $q = 2$ surface. It exceeds even the optimistic prediction from Rice *et al*. (2021) by a factor of 1.5. This intrinsic torque leads only to moderate toroidal rotation values due to the correspondingly large plasma mass. With a predicted 3–9 krad s^{-1} it predicts values similar to the pessimistic case, and one finds slightly lower rotation values at $q = 2$ than those predicted by the scaling in Rice *et al*. (2007). This comparison confirms that a choice of a low rotation case with the low toroidal rotation of 0.5× the model prediction and $T_0 = 5$ Nm, a mid rotation case with the model prediction for the toroidal rotation and $T_0 = 10$ Nm and a high rotation case with the high toroidal rotation of 2.0x the model prediction and $T_0 = 20$ Nm provides good coverage of possible rotation profiles.

3. Vertical stability of the ARC baseline scenario

Vertical stability, or control of the $n = 0$ resistive wall mode, is a fundamental issue for tokamak designs as it both limits the maximum achievable elongation in a particular scenario and constrains the engineering of superconducting poloidal field (PF) coil sets and their respective power supplies. In order to assess the feasibility of vertical control for the ARC machine, a series of iterative studies are performed with the `MEQ-FGE/FGS/FBT` (Carpanese 2021) and `TokaMaker` (Hansen *et al*. 2024) codes, following the generalised procedures outlined in previous work for the SPARC device (Nelson *et al*. 2024). Importantly, the vertical control capabilities of ARC both need to function under the power supply requirements associated with active superconducting coils and be able to demonstrate robustness against the large

https://doi.org/10.1017/S0022377826101421 Published online by Cambridge University Press

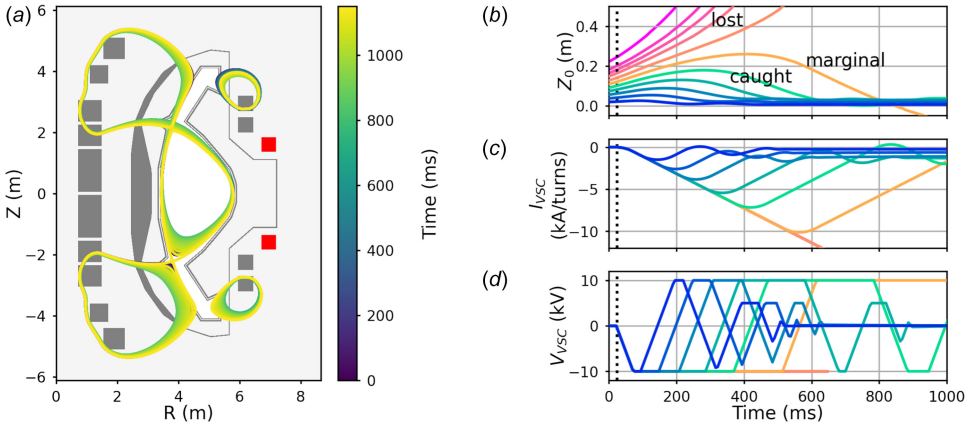


FIGURE 3. (*a*) The separatrix of an example ARC equilibrium evolving through an initial 10 cm vertical displacement towards nominal conditions under vertical control with the PF5 coil (red), as modelled with the TokaMaker code. For a scan of varying initial displacements, the magnetic axis location (*b*), the current used for vertical control (*c*) and the power supply voltage needed to create this current (*d*) are also plotted.

eddy currents that will develop in the thick conducting ARC vacuum vessel and structures. The conducting elements of the ARC vessel and the associated L/R time with inductance L and resistance R are also important for studies of disruption mitigation, as discussed in Sweeney *et al*. (2026). Both codes employed here are capable of solving the integrated temporal dynamics of conductor current evolution and resistive plasma current decay, allowing for accurate assessments of the plasma and machine state during the rapid motion expected during a vertical displacement event. For details on the formulation of these calculations, the reader is directed to expanded discussions in Carpanese (2021), Hansen *et al*. (2024), Nelson *et al*. (2024), Guizzo *et al*. (2024) and Kumar *et al*. (2026). For all calculations presented here, good agreement is observed between the TokaMaker and MEQ-FGE models. Critically, to further increase confidence in the ARC design, both models will be validated upon SPARC data when they become available.

One of the key performance metrics for a vertical control system is maximum controllable displacement $\Delta Z_{\max}$, which characterises the robustness of a vertical control system to spontaneous vertical excursions that may arise from measurement noise, internal MHD events, rapid changes in the plasma current distribution or ELMs (Humphreys *et al*. 2009; Nelson *et al*. 2024). In general, the ability to control displacements of the order of $\Delta Z_{\max}/a_{\text{minor}} \sim 5\,\%$, where a_{minor} is the minor radius of the plasma, corresponds to 'safe' operation in which a tolerable number of vertical excursions are stabilised before leading to a full disruption. As such, the ARC, SPARC, ITER and DEMO designs all target that their control systems be able to, at a minimum, stabilise vertical excursions with initial displacements of $\Delta Z_{\max}/a_{\text{minor}} \gtrsim 5\,\%$ (Humphreys *et al*. 2009; Villone *et al*. 2013; Hahn *et al*. 2020; Nelson *et al*. 2023; Nelson *et al*. 2024). On ARC, this suggests that the vertical stability system must be able to tolerate displacements of at least $\Delta Z_{\max} \sim 6$ cm for safe operation.

To evaluate $\Delta Z_{\max}$ for ARC, equilibria subject to a minimum initial displacement are allowed to evolve in both TokaMaker and MEQ-FGE subject to applied control schemes and self-consistent vessel and eddy currents. An example of this evolution is shown in figure 3(*a*) for a representative ARC equilibrium. Due to the hostile

https://doi.org/10.1017/S0022377826101421 Published online by Cambridge University Press

environment in a high fusion power tokamak, ARC will utilise its poloidal shaping coils for vertical stability control instead of dedicated in-vessel coils. Only the upper and lower PF5 coils (shown in red) are used here to enforce the vertical stability circuit in a split-control configuration. As both TokaMaker and MEQ-FGE allow for explicit design of the target machine, scans of elongation and variations in the ARC shaping coil locations were conducted in parallel to other performance and engineering design tasks. For each iteration of the ARC design, calculations of $\Delta Z_{\max}$ were extracted from scans of ΔZ_0, as shown in figure 3(*b*), to inform design decisions such as the target elongation. As an illustration of this process, figures 3(*c*) and 3(*d*) show the current (I_{VS}) and voltage (V_{VS}) of the vertical stability circuit, respectively, for a particular set of engineering constraints, which may continue to evolve as ARC is constructed. The presented simulation is conducted with an assumption of 100 turns per PF coil, similar to the coil designs of the SPARC tokamak (Nelson *et al*. 2024). This assumption, which impacts the coil self-inductance and required voltage but will not likely substantially change the vertical controllability of ARC plasmas, is expected to change as the power supply systems for ARC are refined. In addition, future iterations of the ARC design may include additional passive stabilising elements to alleviate the burden of vertical stability control on the power supplies. In the simulation shown in figure 3, which includes a 100 ms delay in the control system and a maximum rate of change of 200 $\mathrm{kV\,s^{-1}}$ for the vertical stability power supplies, the I_{VS} slew rate limit of 2.5 $\mathrm{kA\,(ms)^{-1}}$ becomes the limiting parameter for vertical stability control. Using these parameters, $\Delta Z_{\max} \sim 12$ cm is achieved for the ARC baseline scenario, which is approximately twice the expected margin needed for safe operation.

In addition to large scale changes to equilibrium and machine conditions, several potential design trade-offs associated with vertical stability modelling result from specifics of the power supplies that control the coils used for vertical stability control. In particular, variations in the voltage and current slew rates, limits in the maximum power supply voltage and the time delay of filters and diagnostics can all significantly impact the controllability of ARC plasmas. To illustrate this point, sensitivity scans of the voltage slew rate limit and the vertical control filter time are presented in figure 4 for cases where the PF5s are voltage limited, as opposed to the current-limited case presented in figure 3. The requirement that $\Delta Z_{\max}/a_{\mathrm{minor}} > 5\,\%$ be maintained for safe machine operation places direct demands on the engineering parameters associated with the power supplies. Predictions of $\Delta Z_{\max}$ are also sensitive to the number of turns of each PF coil, which was also scanned in this work but remains a free parameter in the present ARC design that will ultimately be set by magnet and power supply design. The precise behaviour of the vertical stability system is expected to change as this value is updated in future iterations of the ARC machine: more turns will reduce the I_{VS} per turn needed for stabilisation but increase the effective inductance and required power supply voltage.

This design of the ARC tokamak also features a liquid immersion blanket with the molten salt FLiBe, which provides cooling to the vacuum vessel, functions both as a tritium breeding medium and a neutron multiplier, and provides neutron shielding to the coils (Hillesheim *et al*. 2026). While the FLiBe blanket provides many benefits for the ARC design, it also introduces another source of uncertainty into machine modelling as the fusion community is still relatively inexperienced in working with the material. To assess the potential impact of a thick FLiBe layer throughout the blanket region, an additional conducting layer with a conductivity of 200 $\mathrm{Sm^{-1}}$, which is estimated to be appropriate for FLiBe at 600 °C based on

https://doi.org/10.1017/S0022377826101421 Published online by Cambridge University Press

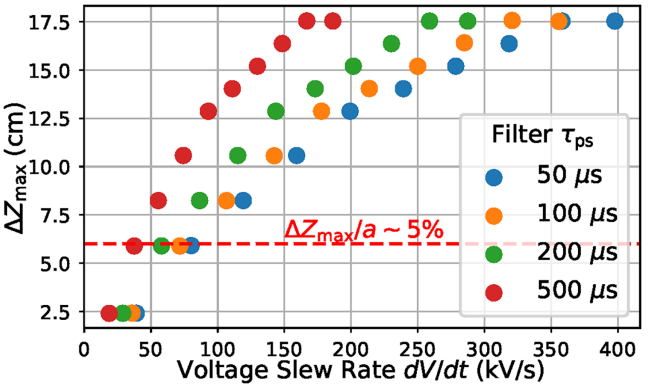


FIGURE 4. The maximum controllable displacement for the ARC baseline design for various filter delay times and voltage slew rates calculated with the MEQ-FGE code. The requirement of $\Delta Z_{max}/a_{minor} > 5\,\%$ where $a_{minor} = 1.18$ m sets engineering limits for power supplies and current systems in ARC.

(Janz 1988), was added to the ARC design in TokaMaker. Since other machine elements are orders of magnitude more conducting, the addition of the FLiBe blanket is found to have little effect on the growth or control of vertical instabilities in ARC. Any induced motion in the FLiBe, while expected to be small compared with the timescale of the magnetic field changes, is ignored in this analysis.

While the precise determination of parameters associated with the vertical stability control system are still being finalised, the scans presented here highlight the impact that predictive vertical stability modelling can have on critical design decisions. Notably, the above results demonstrate that ARC plasmas should be controllable without a dedicated vertical stability coil inside of the vacuum vessel, which could otherwise be complicated to design, install and maintain.

4. Intrinsic 3-D stability

The thermal pressure of every tokamak plasma is ultimately limited by the magnetic pressure of the magnetic field confining the plasma. In practice, this limit can never be reached due to plasma instabilities such as kink and ballooning modes that already become unstable at a much lower thermal pressure or plasma beta, which scales roughly with $I_\mathrm{p}/(a_\mathrm{minor} \cdot B_\mathrm{T})$. This motivates the definition of the normalised plasma beta as $\beta_\mathrm{N} = \beta/(I_\mathrm{p}/(a_\mathrm{minor} \cdot B_\mathrm{T}))$. In a conventional (non-spherical) tokamak the maximum achievable β_N is in the range of roughly 3−6 (Strait 2005), which is generally considered sufficient for a power plant design. However, resistive MHD instabilities such as neoclassical tearing modes can lead to an even lower soft β limit. In this section we investigate the ideal beta limit in § 4.1, which is the β_N at which ideal kink or ballooning modes become unstable, as well as ideal and resistive stability of classical and neoclassical tearing modes in § 4.2.

4.1. *Ideal kink pressure limit*

The Direct Criterion of Newcomb (DCON) code (Glasser 2016) uses the formalism described in Newcomb (1960) to calculate the ideal MHD kink stability of a plasma for toroidal axisymmetric geometry. As a metric for stability, DCON calculates the total energy matrix W_T including the plasma response. If W_T has any

https://doi.org/10.1017/S0022377826101421 Published online by Cambridge University Press

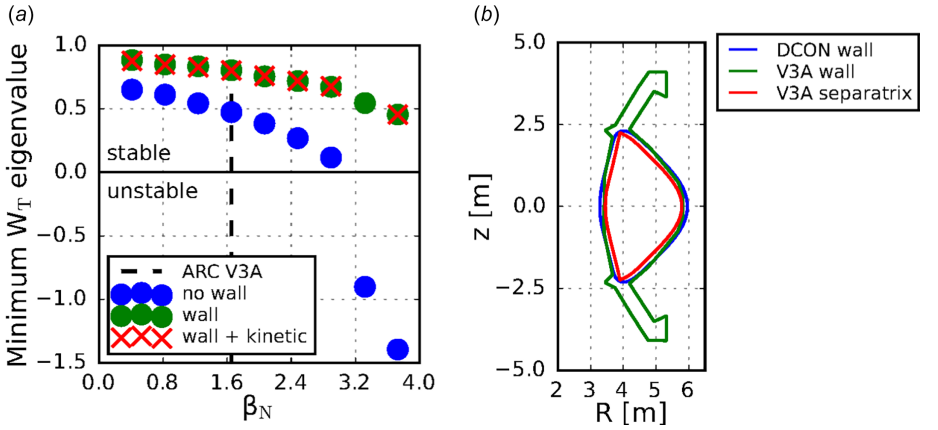


FIGURE 5. (*a*) The minimum of the total response matrix W_T eigenvalues as a function of the normalised beta β_N. Three different cases are shown, the no-wall limit (blue), including a conducting wall (green) and including a conducting wall as well as kinetic effects (red). The vertical dashed black line indicates the β_N of the nominal ARC V3A equilibrium. (*b*) Poloidal cross-section showing the separatrix (red), the first wall (green) and the location of the conducting wall as used in DCON (blue).

negative eigenvalues, then an external mode is unstable. We use this criterion to assess the beta limit for ideal MHD stability of an ARC plasma for $n = 1$.

In order to assess the beta limit, the original ARC equilibrium with $\beta_N = 1.65$ is evaluated as well as a set of equilibria that are generated with TokaMaker by scaling the pressure profile up or down and solving the free-boundary equilibrium with self-consistent bootstrap current. Figure 5(*a*) shows the minimum eigenvalue of the W_T matrix as a function of β_N for three different cases. The blue dots represent the case without a conducting wall and without kinetic effects. The minimum W_T eigenvalues become negative, i.e. the ideal beta limit is reached, at $\beta_N \approx 3.2$ which is roughly a factor of 2 above the nominal value. Hence, we conclude that the ARC plasma is stable and operates at a safe distance from the ideal beta limit. Including a conducting wall can lead to a passive stabilisation of the plasma due to eddy currents in the wall. The DCON code generates a conducting wall with the same shape as the LCFS at a given distance, which we assumed such as to have the conducting wall just behind the first wall of ARC as shown in figure 5(*b*). As expected, the eigenvalue minima are higher in the wall case (green dots) than in the no-wall case (blue dots) meaning that the plasma is even more stable. Including kinetic damping effects (Logan *et al*. 2013; Park & Logan 2017) in addition to the conducting wall (red crosses) has only a negligible effect, of the order of 1 %.

In conclusion, even when assuming the most unstable case without the stabilisation from a conducting wall or kinetic effects, the plasma is still predicted to be far away from the ideal kink beta limit for ARC.

4.2. *Tearing stability*

Tearing modes are deleterious resistive MHD instabilities that grow on rational ($q = m/n$ for poloidal and toroidal mode numbers m and n) surfaces, breaking nested flux surfaces into periodic magnetic islands that can reduce confinement and lead to disruptions. Once grown to sufficient size, tearing modes can induce eddy

https://doi.org/10.1017/S0022377826101421 Published online by Cambridge University Press

currents in the device wall that brake their toroidal rotation and drag on the plasma, potentially leading to mode locking and disruption (de Vries *et al*. 2011; Sweeney *et al*. 2017). In § 4.2.1 we calculate using STRIDE (Glasser & Kolemen 2018) and an analytic proxy for Glasser stabilisation (Glasser *et al*. 1975; Lütjens *et al*. 2001) that ARC is robustly linearly stable to tearing modes, a necessary hurdle for any tokamak fusion plant. In § 4.2.2 we evaluate the nonlinear tearing stability of ARC in the context of other hypothetical plasma scenarios, using a modified Rutherford equation analysis (Rutherford 1973; Hegna 1999; Schlutt & Hegna 2012).

4.2.1. Linear tearing stability

The classical tearing stability index Δ' measures the discontinuity in the perturbed flux at a rational surface, representing the amount of free magnetic energy available for tearing from the perspective of ideal MHD (Furth 1973). The sign of Δ' corresponds to the stability of this surface against linear tearing modes in the low pressure limit (Furth 1973), with $\Delta' > 0$ representing favourable free energy and therefore instability. Using Δ' to probe tearing stability in experimental discharges is an ongoing effort, with past analyses suggesting that linear instability may make mode onset more likely but does not correlate with mode triggering and onset (Kim *et al*. 2025).

The Glasser effect refers to tearing mode stabilisation in tokamak plasmas with good average curvature ($D_R < 0$) and high Lundquist number S (i.e. high temperature). Ideal MHD linear tearing stability analysis can be extended by considering Glasser stabilisation and its modification by thermal transport effects in the resistive region near the rational surface, which can influence the pressure perturbations that lead to tearing mode stabilisation. A critical length scale w_d has been previously derived that is distinct from the resistive layer width δ_s, and in the case where $w_d > \delta_s$, it was found that local flattening of the pressure profile can be used as a proxy for the stabilising influence of thermal transport (Lütjens *et al*. 2001). In other words, when $w_d > \delta_s$, stabilisation due to favourable curvature and thermal transport can be modelled by reducing the free energy available for a tearing mode (Δ') into a new 'effective' tearing stability index Δ_{eff} (Lütjens *et al*. 2001; Fitzpatrick 2025), defined (using a large aspect ratio approximation) as

$$\Delta_{\text{eff}} = \Delta' - \Delta_{\text{crit}} = \Delta' - \sqrt{2}\pi^{3/2}\frac{D_R}{w_d}. \tag{4.1}$$

The critical length scale is given by

$$w_d = 2\sqrt{2}\left(\frac{\chi_\perp}{\chi_\parallel}\right)^{1/4}\frac{1}{(\epsilon s n)^{1/2}}, \tag{4.2}$$

with

$$\chi_\parallel = (\chi_\parallel^{smfp}\chi_\parallel^{lmfp})/(\chi_\parallel^{smfp} + \chi_\parallel^{lmfp}), \tag{4.3}$$

$$\chi_\parallel^{smfp} = (1.581\tau_{ee}v_{te}^2)/(1 + 0.2535Z_{\text{eff}}), \tag{4.4}$$

and

$$\chi_\parallel^{lmfp} = (2R_0 v_{te} r_s)/(\sqrt{\pi} n s w_d) \tag{4.5}$$

(Fitzpatrick 2023). Here, $\chi_\perp$ is the perpendicular energy diffusivity, $\epsilon = a/R_0$, $s = rq'/q$, R_0 is the major radius of the magnetic axis, n is the toroidal mode number, τ_{ee} is the electron-ion collision time, v_{te} is the electron thermal velocity and r_s is the minor radius of the rational surface.

https://doi.org/10.1017/S0022377826101421 Published online by Cambridge University Press

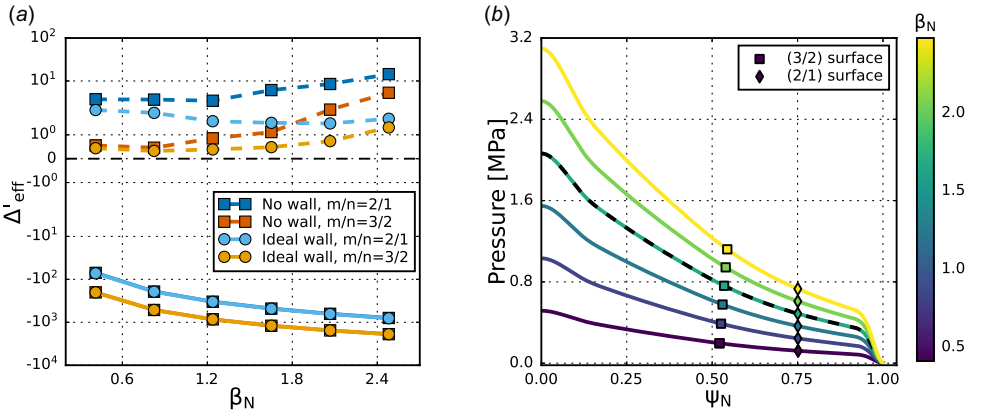


FIGURE 6. ARC β_N scan, showing both increasing Δ' and increasing Glasser stabilisation with β_N; stabilisation effects dominate, leading to a net decrease in Δ_{eff}. (*a*) Dashed lines: STRIDE self-coupled Δ' values. Solid lines: $\Delta_{\text{eff}} = \Delta' - \Delta_{\text{crit}}$. (*b*) V3A baseline scenario at $\beta_N = 1.65$ is marked with a dashed line.

Our previous instability threshold of $\Delta' > 0$ now becomes $\Delta_{\text{eff}} > 0$. Figure 6 shows a β_N scan around the ARC baseline H-mode value of $\beta_N = 1.65$, using Δ' values calculated by STRIDE and Δ_{eff} values calculated via the formalism above. The Δ' values calculated with an ideal conducting wall at a distance of 0.15 times the minor radius are presented alongside the no-wall values (this is the same 'DCON' conducting wall used in § 4.1 and shown in figure 5). At all β_N investigated, all Δ_{eff} values are robustly stable. The stabilising effects of thermal transport and curvature increase with increasing β_N, overpowering the moderate increase in Δ' instability. This presents an optimistic picture for linear tearing stability during a high powered flat top (though such high values of β_N carry increased risk of neoclassical tearing modes).

The exact inductive current profile (j_{ohmic}) in the ARC baseline H-mode is uncertain, due to a variety of factors such as the projected presence of sawtooth oscillations and uncertainties in the magnitude of non-inductive current sources such as the bootstrap current j_{BS}. We chose to model the j_{BS} contribution using Sauter's formula (Sauter *et al*. 1999), and address uncertainties by scanning the bootstrap fraction from 0.25 to 1.25. This scan also has the function of altering the internal inductance ℓ_i from 1.16 at the lowest bootstrap fraction to 0.93 at the highest bootstrap fraction. The j_{ohmic} profile is set such that $q_0 > 1$ in all cases. As seen in figure 7, STRIDE combined with our proxy for Glasser stabilisation finds all $\Delta_{\text{eff}} < 0$. Ideal wall Δ' values are reported alongside the no-wall results. A weak inverse scaling of Δ' with ℓ_i can be seen, since $\partial j_\phi / \partial \psi$ at the $q = 2/1$ and $q = 3/2$ surfaces decreases with increasing j_ϕ profile peakedness.

These predictions suggest stability against linear tearing modes within the bounds of these β_N and ℓ_i scans for the profiles shapes explored when the stabilisation effects of curvature and thermal transport as represented by the proxy Δ_{eff} are included. However, it is important to note that these results are highly sensitive to the current profile shape as more substantially increasing the broadness of the current profile will drive the ideal Δ' more significantly unstable, and conditions with reduced electron temperature and Lundquist number S (e.g. ramp up) may have insufficient curvature and transport stabilisation to maintain $\Delta_{\text{eff}} < 0$. Additionally, excessive radiation

https://doi.org/10.1017/S0022377826101421 Published online by Cambridge University Press

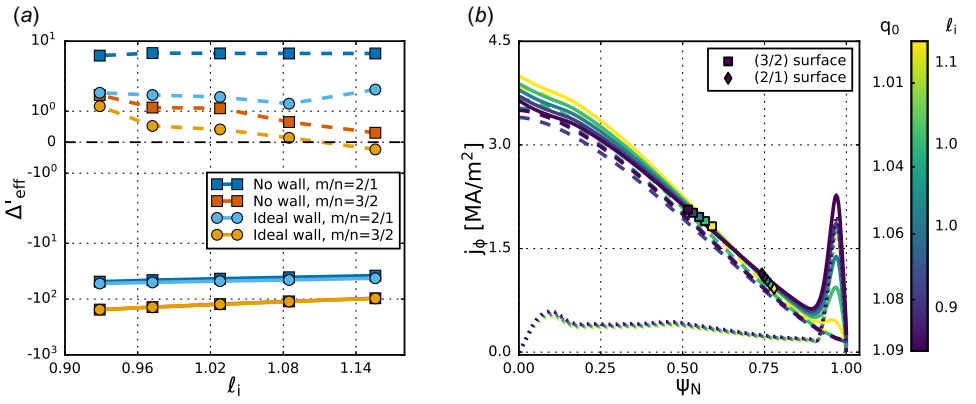


FIGURE 7. ARC ℓ_i scan, showing weak dependency of the 3/2 Δ' on ℓ_i and robust Glasser stabilisation. (*a*) Dashed lines: STRIDE self-coupled Δ' values. Solid lines: $\Delta_{\text{eff}} = \Delta' - \Delta_{\text{crit}}$. (*b*) V3A baseline scenario $\ell_i = 0.97$. Dashed lines: j_{ohmic} profiles. Dotted lines: scaled j_{BS} profiles as calculated by the Sauter formula (Sauter *et al*. 1999).

may drive the current profile toward instability due to current contraction in the core or edge (Pucella *et al*. 2021). Further investigation is planned to probe off-normal and more dynamic scenarios where instability may be possible, and SPARC will provide a vital testbed for validating these models as well as testing ways to manipulate the current profiles in order to improve predictions of linear tearing stability on ARC. Further studies also focus on a proper uncertainty assessment of Δ' and Δ_{eff}.

4.2.2. Nonlinear tearing stability

While the ARC equilibrium configuration is linearly stable to tearing modes, transient plasma instabilities including sawteeth and toroidal Alfvén eigenmodes may cause reconnection at rational surfaces in the core. This process can 'seed' neoclassical tearing modes (NTMs), which are driven nonlinearly unstable by the local loss of bootstrap current that results from pressure flattening inside the island separatrix. To analyse NTM stability in ARC, we can apply the toroidal modified Rutherford equation (Hegna 1999; Schlutt & Hegna 2012; La Haye 2006, 2017), which models the evolution of a single tearing mode's width 'w' in normalised flux coordinates after it has exceeded the linear layer width $\delta_s \propto S^{-1/3}$

$$\frac{1.22^{-1}}{\eta*}\frac{\mathrm{d}w}{\mathrm{d}t} = \Delta'\left|\frac{w}{2}\right|^{-2\alpha_-}\sqrt{-4D_I} + \frac{w}{w^2 + 1.7/0.5w_d^2}1.7D_{nc} + \frac{1}{w + 1.7/(0.3(1+\alpha_+))w_d}\frac{1.7D_R}{\alpha_+ - H} + \Delta_{pol}. \tag{4.6}$$

Here, $\eta^*[s^{-1}]$ is the resistive diffusion coefficient in normalised flux space (Hegna 1999), D_I and D_R are the Mercier and resistive interchange stability criteria, respectively (Glasser *et al*. 1975), $\alpha_\pm = 1/2 \pm \sqrt{-4D_I}$, $H = 1/2 - \sqrt{D_R - D_I}$ (Glasser *et al*. 1975), $D_{nc} \sim (J_{boot}/\langle J_\parallel \rangle)q/q'$ (Hegna 1999; La Haye 2017) captures the neoclassical tearing drive and w_d is the characteristic island width beneath which cross-field transport prevents any pressure perturbation forming in the island (Fitzpatrick 1995; Schlutt & Hegna 2012). Further, $\Delta'|w/2|^{-\alpha_-}\sqrt{-4D_I}$ is the

https://doi.org/10.1017/S0022377826101421 Published online by Cambridge University Press

finite-pressure contribution from the equilibrium tearing stability parameter Δ' (Kotschenreuther, Hazeltine & Morrison 1985; Hegna 1999) and Δ_{pol} represents the stabilising effect (Waelbroeck 2005; Ishizawa *et al*. 2012) of the two-fluid ion polarisation current, which we will exclude as its sensitivity to the motion of the tearing mode relative to the bulk plasma (La Haye *et al*. 2022) renders it somewhat unreliable for suppressing NTMs. Across all linearly stable ARC-like high-field H-mode scenarios the first and third terms in (4.6) will keep $\mathrm{d}w/\mathrm{d}t$ negative in the small-island limit. However, if w exceeds some marginal width $w_m \sim w_d$, the neoclassical tearing drive can turn $\mathrm{d}w/\mathrm{d}t$ positive and an NTM will grow. This requires a seed island of size $w > w_m$ at the rational surface to initiate growth.

Some degree of island seeding will likely occur in ARC, due to the prevalence of sawteeth (Brennan *et al*. 2007; Yu *et al*. 2019) which are common in high-temperature inductive plasmas operating at low safety factor. One strategy to minimise the risk of NTM onset in the presence of seeding, however, is to identify and operate in scenarios that have large marginally stable island widths for all core poloidal and toroidal m, n modes (Benjamin *et al*. 2026). We can quantify this metric using the minimum marginally stable island width w_m^* defined as $w_m^* \leq w_m(m, n)$ for all m, n of interest.

Minimum marginally stable island width calculations on 12,452 Monte Carlo generated high-field ARC-like equilibria (normalised to a minimum 400 MW fusion power) suggest that the passive NTM stability of a FFP can be strongly influenced with scenario design alone (Benjamin *et al*. 2026). ARC marginally stable island widths from the l_i scan (figure 7) were overlaid on this synthetic equilibrium database in figure 8. The principal physics term dominating the trend in w_m^* across the database was the bootstrap drive D_{nc}, with smaller bootstrap drive strongly correlated with larger minimum marginally stable island widths. Full stabilisation ($\mathrm{d}w/\mathrm{d}t < 0$ for all w) occurred for 17 % of cases, located in the top left of figure 8. For the internal-mode ARC cases, the current profiles with higher internal inductance demonstrated increased NTM stability through w_m; a more peaked current profile shifted core rational surfaces outwards, reducing local pressure gradient and hence D_{nc}. When compared with the rest of the database, the ARC internal-mode marginally stable island widths lie on the more unstable side of the D_{nc} trend. This is partially due to a systematic difference in current profile shape generation for ARC versus the rest of the synthetic database (Benjamin *et al*. 2026). Adding an ideal conducting wall at 0.15 times the minor radius reduced ARC's $m, n = 2, 1$ w_m values by up to an order of magnitude while leaving $m, n = 3, 2$ w_m values largely unchanged. This was primarily because $m, n = 2, 1$ Δ' showed greater sensitivity to the vacuum region than the 3, 2 Δ' (see figure 7).

Overall, with a marginally stable island width of the order of just 0.1 % of the normalised poloidal flux, this raises concern that even very small seeding islands can grow into an NTM. This general conclusion is somewhat in line with empirical scalings of NTM onset, which suggest that the β_{N} threshold for NTM onset scales with the normalised ion Larmor radius ρ^* (La Haye *et al*. 2000; Buttery *et al*. 2000; Hender *et al*. 2004). For ARC the predicted ρ^* calculated on the magnetic axis is about 0.0016, which is a factor of 4 lower than the lowest ρ^* data included in the aforementioned studies. If those linear scalings were valid at that low ρ^*, then the predicted critical $\beta_{\mathrm{N}} = 0.5$ would be well exceeded in the nominal ARC scenario with $\beta_{\mathrm{N}} = 1.65$. This scaling also competes with the scaling of seed island widths, which decrease as well with decreasing ρ^* (La Haye *et al*. 2000). At low ρ^* such as at ARC, this is predicted to lead to a very sharp increase of the critical β_{N} for NTM

https://doi.org/10.1017/S0022377826101421 Published online by Cambridge University Press

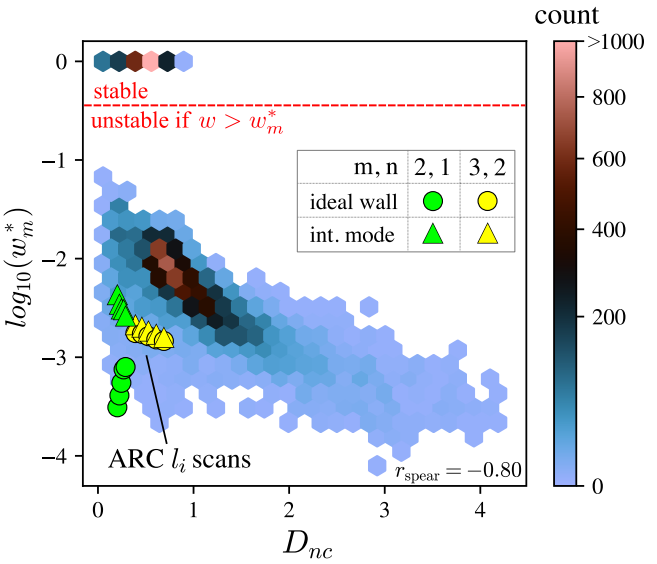


FIGURE 8. Two-dimensional histogram of minimum marginally stable island widths vs bootstrap drive D_{nc} at the least stable mode, for ARC-like H-mode equilibria. Seventeen per cent of cases in the top left corner are fully stabilised. Since w_m^* is not defined for stables cases, they are included as $w_m^* = 1$. r_{spear} is Spearman correlation coefficient. The labelled ARC cases describe $m, n = 2, 1$ (green) and 3, 2 (yellow) w_m values calculated from the current profiles presented in figure 7. STRIDE was used to compute Δ' with an ideal wall at 0.15 times the minor radius, as well as internal-mode Δ' to compare with the database.

onset, however, the exact ρ^* where this reversal of the trend occurs depends strongly on physics assumptions (La Haye *et al*. 2000; Buttery *et al*. 2000) and no data exist at that ρ^* to validate predictions. Also in contrast to that, it is believed that in an FPP sawteeth become more stable due to fast ion effects leading to slower sawtooth cycles and larger sawteeth, which lead to larger seed islands.

Furthermore, the critical β_N for NTM onset is also found to reduce for decreasing plasma rotation (Buttery *et al*. 2008; La Haye & Buttery 2009; La Haye *et al*. 2010, 2011). In Bardóczi *et al*. (2025) it is identified that in particular the differential rotation between the $q = 1$ surface and the NTM resonant surface is critical. This effect can be further amplified by error fields or intentionally applied 3-D fields that brake the plasma and can destabilise NTMs when operating close to the β_N threshold (Buttery *et al*. 2011). As mentioned already in § 2, due to the absence of external torque the plasma rotation in an FPP will be fairly small and be dominated by intrinsic rotation, which cannot be reliably predicted.

Ongoing experimental database studies and simulations in M3D-C1 will attempt to correlate a likelihood of tearing onset with these marginally stable island widths as well as predict seed island widths caused by sawteeth. As tearing mode dynamics, seed islands and their interactions are theoretically challenging and no data exist to validate those models in FPP like conditions, making predictions about the threat of NTMs for FPPs a challenging issue. The SPARC tokamak with a normalised Larmor radius ρ^* of approximately 0.003 bridges a large gap in experimental data towards FPP conditions. These new data from SPARC will be relied upon to test

https://doi.org/10.1017/S0022377826101421 Published online by Cambridge University Press

both the predictive capability of these analyses, and to empirically quantify the tearability of high-field, fully inductive burning plasmas. SPARC also has a set of 3-D coils able to study the effect of 3-D fields on tearing stability.

5. Error fields

In this section we use an empirical model to predict the $n = 1$ error field that leads to mode locking and a disruption in the ARC scenario. Based on the finding, a physics basis to inform the design of EFCCs optimised for $n = 1$ error field correction is built. The goal of this section is to map a large coil geometry space that can serve as a basis to guide the design of EFCCs for ARC, identify the most restricted and most flexible components of the design and finally provide a potential coil design based on those findings. Although the capability to correct $n = 1$ error fields is the only criterion that guides the design of the EFCCs, their potential for other applications such as $n = 2$ error field correction and suppression of ELMs is addressed as well. Initially in addition to picture-frame coils, individual coil filaments that only extend in horizontal or vertical direction were considered due to their simpler geometry and the fact that they take less space. The latter got quickly deselected due to their weak coupling, and hence this work focuses purely on picture-frame coils. They are the standard coil variant used for error field correction and 3-D physics in today's tokamaks and are also planned for ITER (Foussat *et al*. 2010) and SPARC (Logan *et al*. 2022) due to their versatility and easy installation around ports.

The analysis of this section uses a modelling framework of DCON, the Generalised Perturbed Equilibrium Code (GPEC) and Perturbed Equilibrium Non-Ambipolar Transport Code (PENTRC). The two main metrics being used are the overlap of the external field with dominant mode of the plasma δ_{core} as well as the maximum correctable error field δ_{max}. The δ_{core} metrics describes how well an externally applied perturbation field couples to the dominant mode of the plasma and hence gets amplified. The δ_{max} metrics represents the largest error field that can still be corrected based on a simple model that includes the reduction of the critical error field due to the neoclassical toroidal viscosity (NTV) torque of the applied external field. The framework and the metrics are described in detail in the Appendix A.

5.1. *Error field prediction*

In Logan *et al*. (2020) an empirical scaling of the mode locking probability for a given $n = 1$ error field was developed based on a multi-machine database. Figure 9 shows this prediction of the module locking probability for the kinetic ARC equilibrium as a function of δ which is the dominant $n = 1$ error field component normalised to the toroidal field. The uncertainty band is representing the range of deviation from the prediction for up to 20 % variation in the input parameters with significant potential for uncertainty, which are the electron density at the $q = 2$ surface $n_e = 2.3 \times 10^{20}\ \text{m}^{-3}$, the normalised plasma beta $\beta_N = 1.65$ and internal inductance $l_i = 1.19$. No uncertainty is assumed for major radius R_0 and the toroidal field B_T. In addition, SPARC (full field/current L-mode scenario with $R_0 = 1.85\ \text{m}$, $B_T = 12.16\ \text{T}$, $n_e = 1.12 \times 10^{20}\ \text{m}^{-3}$, $\beta_N = 1.0$, $l_i = 1.1$) and ITER (full field/current H-mode scenario with $R_0 = 6.2\ \text{m}$, $B_T = 5.3\ \text{T}$, $n_e = 0.98 \times 10^{20}\ \text{m}^{-3}$, $\beta_N = 1.8$, $l_i = 1.0$) scenarios are included for comparison. The scaling predicts a stronger sensitivity of mode locking on a given error field amplitude for ARC as compared with ITER, i.e. a higher chance of mode locking for a given normalised error field. However, compared with SPARC the chances for mode locking are smaller at any given normalised error field. This suggests that the predicted error

https://doi.org/10.1017/S0022377826101421 Published online by Cambridge University Press

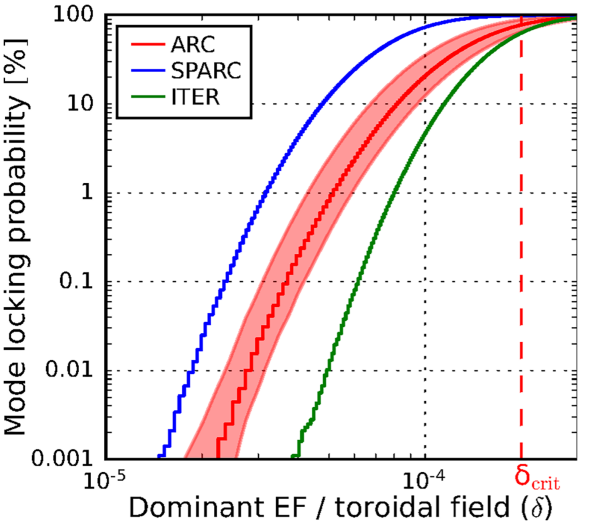


FIGURE 9. Empirical extrapolation of the mode locking probability as a function of the dominant $n = 1$ EF amplitude normalised to the toroidal field. The ARC scenario (red) is compared with predictions for SPARC (blue) and ITER (green). The uncertainty band for the ARC scenario represents a 20 % variation of density, normalised plasma beta and internal inductance put into the scaling law.

field that imposes a reasonably low risk for mode locking between 0.01 % and 0.1 % and consequent requirements for engineering precision is within the existing range of experience from SPARC and ITER.

For further calculations in the following sections, we deduce the critical error field, i.e. the error field that according to the scaling leads to mode locking (near 100 % mode locking probability in figure 9), to be $\delta_{crit} = 2 \times 10^{-4}$.

5.2. *Design of error field correction coils*

Firstly we focus on a singular row of picture-frame coils that can be defined in the poloidal plane as shown in figure 10 by the distance d between the centre of the coil and the plasma surface, their extent in the poloidal plane here dubbed height h, their poloidal angle or rotation angle θ_{rot} measured from the LFS midplane in counter-clockwise direction and the tilt angle with respect to the plasma surface θ_{tilt} in counter-clockwise direction in the poloidal plane.

Scans of those four different coil parameters are shown in figure 11 for a single row of coils. The top row shows contours of the core overlap normalised to the toroidal field δ_{core} (a) for a scan of the rotation θ_{rot} and tilt θ_{tilt} angles that has been performed at constant coil distance $d = 2$ m and coil height $h = 14m$. The θ_{rot} scan spans from the midplane at $\theta_{rot} = 0°$ to the HFS at $\theta_{rot} = 0°$. Due to the up–down symmetry of the ARC equilibrium only the range above the midplane is covered. The θ_{tilt} scan spans from a coil parallel to the plasma surface at $\theta_{tilt} = 0°$ to a coil perpendicular to the plasma surface $\theta_{tilt} = 90°$. At $\theta_{tilt} = 0°$, the core overlap with either normalisation maximises off-midplane at around $\theta_{rot} = 45°$ and at those locations the overlap also maximises when the coil is parallel to the plasma surface. For coils located near the midplane around $\theta_{rot} = 0°$ the overlaps surprisingly increase as the coil is being tilted to be more perpendicular to the plasma.

https://doi.org/10.1017/S0022377826101421 Published online by Cambridge University Press

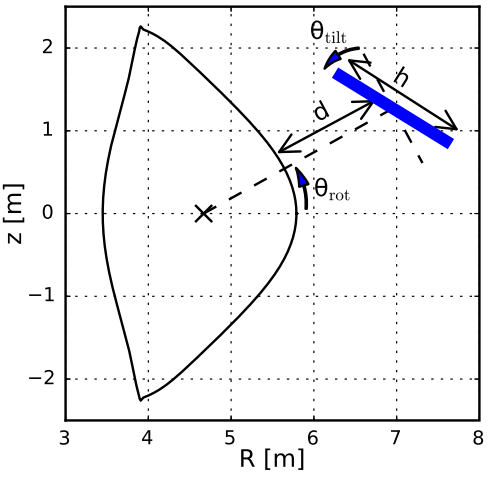


FIGURE 10. Visualisation of the geometric coil parameters in a poloidal cross-section showing the plasma separatrix (black) and a window-frame coil (blue).

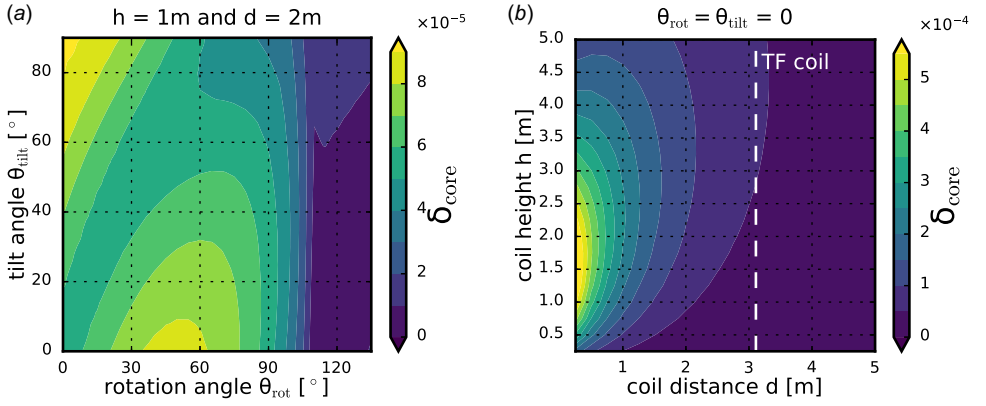


FIGURE 11. Scans of core overlap normalised to the toroidal field δ_{core}. Panel (*a*) covers scans of the rotation and tilt angles of the coil at constant height and distance and (*b*) covers scans of the height and distance of the coil at constant rotation and tilt angles. Dashed white line in (*b*) indicates the distance from the plasma surface to the outer boundary of the toroidal field coils.

When the coil is within 2 m of the plasma surface, clear optima can be seen in the coil height in figure 11(*b*). This can be explained by the height of the coil being close to the half-wavelength of the dominant mode. At a distance of 1 m a coil of approximately 2.3 m height has the largest overlap with the dominant mode, but the optimum in terms of δ_{core} is shifted towards larger coils around the farther away they are. At distances further away from the plasma, the dependence of δ_{core} on the coil length becomes weaker and eventually vanishes.

One constraint for the 3-D coils is that they are being installed inside the cryostat but outside the toroidal field coils (TF-coils) due to the lack of space closer to the plasma. Dashed white lines provide a rough estimate of the outer boundary of

https://doi.org/10.1017/S0022377826101421 Published online by Cambridge University Press

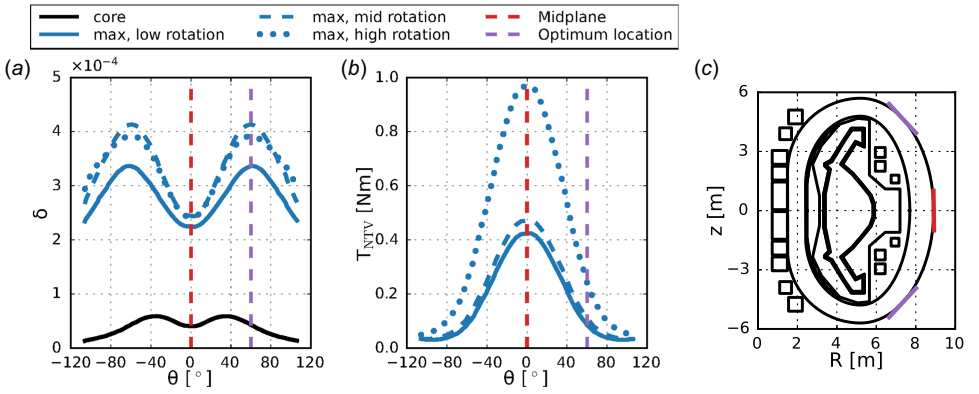


FIGURE 12. (*a*) The core overlap δ_{core} and maximum correctable error field δ_{max} metrics as well as (*b*) NTV torque T_{NTV} as a function of θ for the three different rotation cases. (*c*) Poloidal cross-section illustrating the location scan θ of the 3-D coils mounted on the TF-coils. In addition, the central solenoid (vertically stacked black boxes on the HFS), shaping coils (remaining black boxes) and vacuum vessel are included. Vertical dashed lines in (*a,b*) correspond to the coils in (*c*).

the toroidal field coils. At this distance, the coil length has no optimum within a reasonable range of coil heights, and thus larger is better due to the overall larger field generated as seen in the plot of δ_{core}. From here on we focus on 3-D coils installed directly on the outside of the TF-coils due to simplicity of mounting them there and the importance of minimising the distance to the plasma.

5.2.1. Coil location

To further narrow down the best location of the 3-D coils mounted on the TF-coils, a scan along the TF-coils is performed. This of course removes the tilt angle as a parameter of freedom and it is set by the shape of the TF-coils at the mounting location. Figure 12(*c*) shows a poloidal cross-section including noteworthy 3-D coil locations. The coil metrics as a function of θ show distinct characteristics in figure 12(*a*). As generally expected for typical positive triangularity plasma shapes, δ_{core} (black line) is largest near the LFS midplane. The maxima are at approximately $\theta = \pm 38°$ and at the midplane (red vertical line and coil) δ_{core} is approximately 30 % lower. The maximum correctable error field δ_{max} peaks further off-midplane at around 60° for all rotation cases as indicated by the blue lines. The peaks exist despite the reduced δ_{core} at those locations due to the also strongly reduced NTV torque for coils at those locations (see figure 12(*b*)). The exact location of the δ_{max} optimum and its benefit over a row of midplane coils are set mainly by NTV torque profile, which in turn depends strongly on the kinetic equilibrium.

Overall, these scans suggest that the exact location of coils mounted on the TF-coils can have a significant impact on the capability to correct error fields. The optimum location is generally off-midplane on the LFS at 40°–80° and can be increased by a factor of 2.

5.2.2. Coil height

For the midplane coil (red) and the off-midplane coils (purple) identified in figure 12, scans of the coil height h are performed as shown in figure 13. The core overlaps δ_{core} in figure 13(*a*) show a near linear increase with the coil height

https://doi.org/10.1017/S0022377826101421 Published online by Cambridge University Press

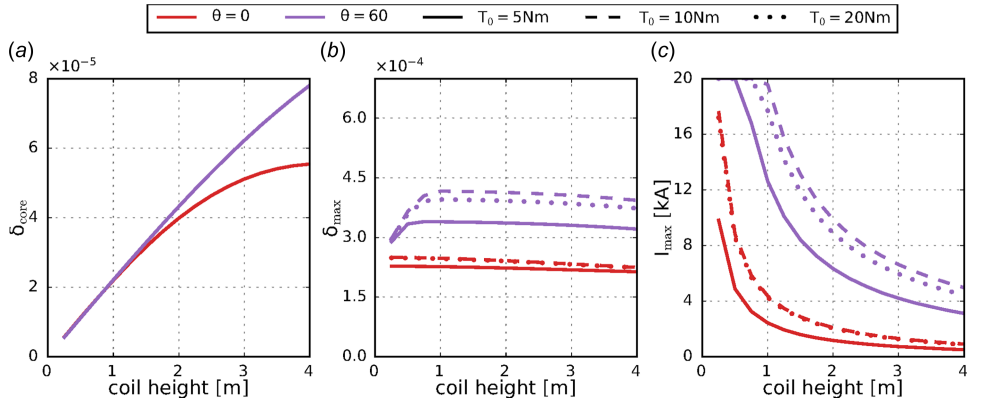


FIGURE 13. (*a*) Core overlap δ_{core}, (*b*) maximum correctable error field δ_{max} and (*c*) required coil current I_{max} at an intrinsic torque of 5, 10 and 20 Nm as a function of the coil height for the midplane (red) and off-midplane (purple) coil identified in figure 12.

as expected due to the linearly increasing perturbation field at the cost of slightly less efficiency. The maximum correctable error field δ_{max} for intrinsic torques of $T_0 = 5$, 10 and 20 Nm shown in figure 13(*b*) has only a negligible dependence on the coil height within a reasonable range for all cases beyond $h = 0.6$ m. The coil currents I_{max} required to reach those δ_{max} values are shown in figure 13(*c*), and have a strong nonlinear dependence on the coil height. A steep fall-off between $h = 0$ m and approximately 1.5 m can be seen in all cases and becomes especially important for the off-midplane coils. In combination with the weak dependence of δ_{max} one can see that going beyond approximately $h = 2$ m has only minimal benefits reducing the power supplies demands a bit at the cost of slightly reducing δ_{max}.

In conclusion, the coil height is also rather flexible beyond a lower limit of approximately 1.5 m to avoid high power supply demands.

5.2.3. Number of coil rows

Optimising coil geometries was so far only applied to single rows of coils. However, it can be beneficial to have multiple rows of coils which allows for a better control of the poloidal mode spectrum and a larger field in sum. In the following we consider three different sets of window-frame coils. The first set of coils consists of a single row of coils on the LFS midplane with a coil height of 4 m (see location of red coil in figure 12(*a*)). The second set consists of two rows of off-midplane coils at the locations optimised to achieve the maximum correctable error field (see location of purple coils in figure 12(*a*)) with a coil height of 2 m. The third set is a combination of all three rows of coils. The increased coil height of the midplane coil is chosen such as to accommodate for possible ports that the vertical and horizontal legs of the coils cannot intersect with.

The metric used in the comparison is again the maximum error field that can be corrected before the NTV torque effect takes over at higher EFCC currents (turning point in figure 19). For the coil sets with multiple rows of coils the differential phase angles between the individual coil rows $\Delta\Phi$ and the ratio of coil current amplitudes in each row have a great impact on the maximum correctable error field. Therefore, differential phase scans have been performed in the range of 0–2π and amplitude ratio scans in the range of 0–10 for all coil sets. An additional constraint is that only

https://doi.org/10.1017/S0022377826101421 Published online by Cambridge University Press

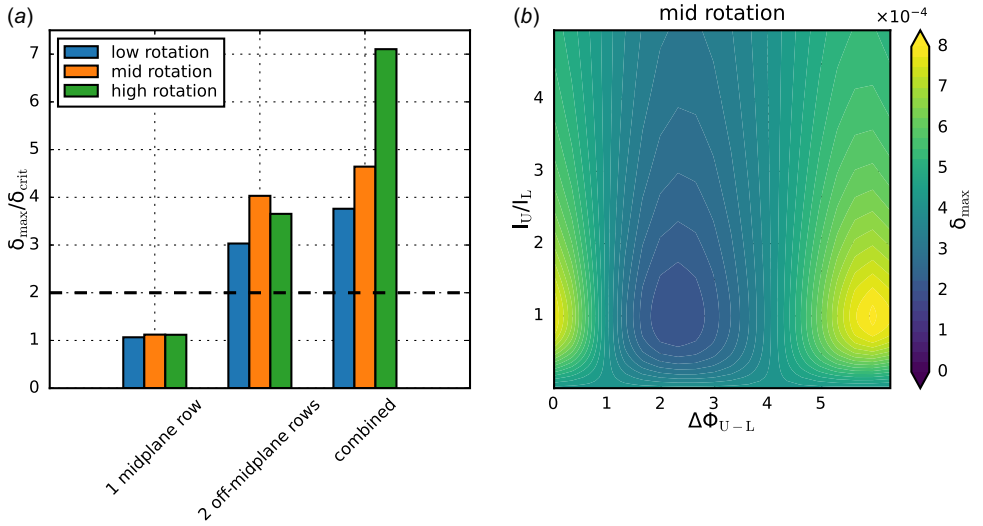


FIGURE 14. (*a*) The maximum correctable $n = 1$ error field δ_{max} relative to the critical error field δ_{crit} is shown for the three different design choices related to a row of LFS midplane coils with 4 m height and two off-midplane coils with 2 m height (see coils in figure 12(*c*)) for the three different rotation cases. The maximum coil current in any of the coils rows is limited to 20 kA. The dashed line indicates $\delta_{max}/\delta_{crit} = 2$. (*b*) The impact of the differential phase angle $\Delta\Phi_{U-L}$ and the coil current amplitude ratio between upper and lower off-midplane coil rows on δ_{max} for the high torque case.

cases with less than 20 kA in each coil are being considered. For each coil set, the largest possible maximum correctable error field relative to the critical error field is shown in figure 14(*a*) for the three cases of low, mid and high rotation and torque (different colours). The dashed line indicates $\delta_{max}/\delta_{crit} = 2$ which has been deemed a sufficient capability for the EFCC design of SPARC (Logan *et al*. 2022). This criterion is not met for any of the rotation cases of the coil design with only the LFS midplane coil. Due to strong the NTV drive of midplane coils relative to their overlap with the core dominant mode (see figure 12), these coils seem unlikely to be suitable for error field correction on their own for most plasmas. The low NTV drive of off-midplane coils enables them correct error fields up to 8 times higher than the critical error field depending on the rotation. When combined with the off-midplane coils, the midplane row is actually enabling even higher error fields to be corrected. The dependence of δ_{max} on $\Delta\Phi$ and the amplitude ratio in the case of the design with two off-midplane rows is shown in figure 14(*b*) for the mid rotation case. The choice of the right $\Delta\Phi$ is critical and highlights the importance of having enough coils in each row to be able to adjust $\Delta\Phi$ accordingly. For $n = 1$ error field correction the minimum number of coils is 4 per row with individual power supplies to enable that. The maximum of δ_{max} is at an amplitude ratio of 1 between the upper and lower rows of coils, which is not surprising given the up–down symmetry of the ARC equilibrium and the symmetrical locations of the two coil rows.

The conclusion of this comparison is that a single row of midplane coils appears to be generally incompatible with error field correction due to the high NTV torque induced by it. On the other hand, even when limited to below 20 kA coil currents, the use of two off-midplane rows of coils at optimised locations can enable compensation

https://doi.org/10.1017/S0022377826101421 Published online by Cambridge University Press

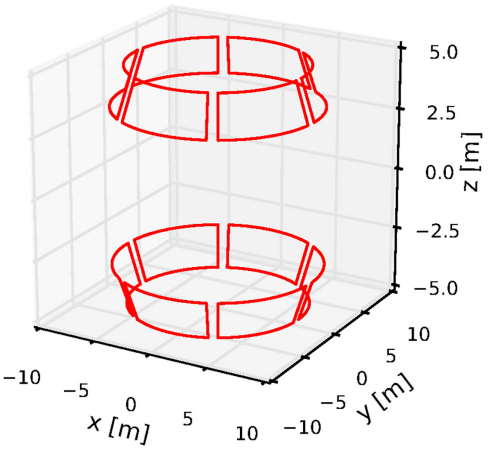


FIGURE 15. Three-dimensional depiction of two rows of off-midplane EFCCs at optimised locations and coil height mounted on the toroidal field coils.

of the extrapolated critical error field with at least a factor of 3 overhead even in the pessimistic low rotation case. And while there is a significant increase in the maximum correctable error field when additionally using the midplane row of coils, we conclude that this is not necessary for reliable error field correction.

5.2.4. Discussion of a design recommendation

The analysis in the previous sections suggest that a design with only a midplane row is high risk due to the strong NTV drive of coils at the LFS midplane in most plasmas. And while a 3-row design with a midplane row and off-midplane rows can significantly increase the maximum correctable error field, the 2-row design consisting only of off-midplane coils is a good compromise between maximum correctable error fields and the complexity of the coil set. Such a set is shown in figure 15. The coil height used is 2 m in order to reduce the demands to power supplies. The coil heights could be further reduced to as low as 1 m and still meet the $\delta_{max}/\delta_{crit} = 2$ criterion at the cost of approximately 50 % higher coil current amplitudes up to 15 kA.

Note that the optimisation of the coils is very sensitive to the NTV torque induced by coils, and the NTV torque in turn is very sensitive to the toroidal current and rotation profile predictions, which are highly uncertain. This could motivate further studies in future design iterations for ARC focusing on more dedicated rotation predictions by performing momentum transport calculations including the NTV torque. As it can be seen in figure 15 the toroidal gaps between neighbouring coils are, with only 6°, rather narrow. The impact of the toroidal gap size is another parameter of freedom that has not been investigated in this study, but will be included when approaching a more matured ARC design. Its main effect would be the creation of higher n side bands with increasing gap size due to spatial aliasing, which can have an effect on the maximum correctable error field via the NTV torque.

5.3. *Potential for other applications*

5.3.1. The $n = 2$ error field correction

The cross-machine model for error field predictions (Logan *et al*. 2020) shows that the critical $n = 2$ error field leading to mode locking and a disruption is of similar

https://doi.org/10.1017/S0022377826101421 Published online by Cambridge University Press

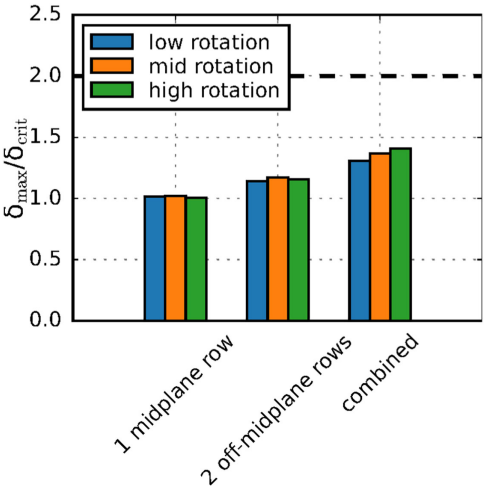


FIGURE 16. The maximum correctable $n = 2$ error field δ_{max} relative to the critical error field δ_{crit} is shown for the three different design choices related to a row of LFS midplane coils with 4 m height and two off-midplane coils with 2 m height (see coils in figure 12(*c*)) for the three different rotation cases. The maximum coil current in any of the coils rows is limited to 20 kA. The dashed line indicates $\delta_{max}/\delta_{crit} = 2$.

size as the critical $n = 1$ error field. And not only can $n = 2$ error fields lead to disruptions, but it can also couple to $n = 1$ error fields and reduce the critical error fields of the latter. Yet, $n = 2$ error field correction was not included in the optimisation since most large error fields are $n = 1$, such as misalignment of the central solenoid or PF coils. In order to do $n = 2$ error field correction at least 6 coils are required in each row of coils in order to allow to adjust the absolute orientation of the $n = 2$ field.

An assessment of the capability to correct $n = 2$ with the three different EFCC sets identified in 5.2 is summarised in figure 16 for the three rotation scenarios. Similar to the $n = 1$ error field, the $n = 2$ error field cannot be corrected with only the midplane row of EFCCs due to the overwhelming NTV torque. And while the other EFCC sets utilising off-midplane coils are capable to some degree of error field correction, neither meet the desired design criterion of $\delta_{max}/\delta_{crit} = 2$. So if $n = 2$ error field correction becomes more relevant for the ARC design, it should be included in future updated EFCC design optimisations.

5.3.2. Suppression of edge-localised modes

Another application of 3-D fields are resonant magnetic perturbations (RMPs) at the edge of the plasma, which can lead to a complete suppression of ELMs (Fenstermacher *et al*. 2025). While naturally ELM-free regimes may be preferable, access to such regimes (including RMP ELM suppression) cannot be predicted with high confidence. Therefore, RMP ELM suppression can still be considered as a possible alternate method among others for avoiding large edge transients. Achieving RMP ELM suppression is not prioritised in the optimisation process for the 3-D coils, rather we simply assess whether the 3-D field coil set-up optimised for $n = 1$ error field correction has the potential to also suppress ELMs.

https://doi.org/10.1017/S0022377826101421 Published online by Cambridge University Press

A recent cross-machine database study has compared different 3-D field metrics in terms of how well they serve as an access criterion for RMP ELM suppression independent of their toroidal mode number (Logan *et al*. 2025). There the overlap between the externally applied field and dominant mode leading to edge resonance δ_{edge} is identified as the most suitable metric to describe the access to RMP ELM suppression and to inform future 3-D coil designs. In this study, an edge overlap of $\delta_{\text{edge}} = 7.5 \times 10^{-4}$ was large enough to cover 95 % of the ELM suppression cases and is therefore used as a design criterion in the following analysis. Some classes of models (e.g. Snyder *et al*. 2012; Hu *et al*. 2020) propose additional criteria such as a particular relationship between the location of resonant surfaces and the pedestal top location. Such criteria can potentially be satisfied via relatively small modifications of q_{95}. However, there is significant uncertainty about whether ARC density, rotation and exhaust solutions are compatible with RMP ELM suppression. And while recent progress has been made in achieving RMP ELM suppression in FPP-like double-null configurations in MAST-U and DIII-D, it is not known yet what makes it difficult in the first place in those shapes.

Hence, the conclusions drawn here are only on whether or not the 3-D coil set-up is capable of producing large enough fields required for RMP ELM suppression, and not on detailed development of an RMP ELM suppression scenario in ARC plasmas. SPARC operation should provide significant new information on the applicability of RMP ELM suppression to ARC.

We include the three designs consisting of the midplane coil, the two off-midplane coils, or all three coil rows combined mounted on the TF-coils as described in § 5.2 and displayed in figure 12(*c*). And since the current designs of the 3-D coil set-ups consist of 6 individual coils in each toroidal row of coils, we can only consider ELM suppression with $n = 1, 2$ or 3 fields. The edge overlap δ_{edge} includes interaction with the resonant surfaces closest to the pedestal top. For $n = 1$ that is the $q = 3/1$ surface, for $n = 2$ that are the $q = 6/2$ and $q = 7/2$ surfaces, and for $n = 3$ that are the $q = 9/3$ and $q = 10/3$ surfaces. The location of these resonant surfaces relative to the pedestal top can be seen in figure 2(*c*). For the coil sets with multiple rows of coils the differential phase angles between the individual coil rows $\Delta\Phi$ and the ratio of coil current amplitudes in each row impact the poloidal mode spectrum of the applied perturbation field and hence change the overlap with the dominant modes in the edge. Therefore, differential phase scans have been performed in the range of $0–2\pi$ and amplitude ratio scans in the range of 0–10 for all coil sets. Figure 17(*a*) summarises the largest achievable δ_{edge} by optimising the differential phases and amplitude ratios for all coil sets and toroidal mode numbers given a field with an average 1 kA coil current amplitude across all coil rows. As expected δ_{edge} tends to drop for an increasing toroidal mode number due to the stronger radial falloff of the perturbation field amplitude with poloidal, and consequently also toroidal, mode numbers. In figure 17(*b*) the average coil current amplitudes required to meet the $\delta_{\text{edge}} = 7.5 \times 10^{-4}$ criteria are shown. This ranges from 6 kA for $n = 1$ with the combined coil set-up to approximately 60 kA for $n = 3$ with only the off-midplane coils. While for $n = 1$ the required coil currents are with just 6–15 kA, in a range comparable to today's devices, it is generally advisable to not use $n = 1$ field for ELM control. That is due to the significant $m/n = 2/1$ component that $n = 1$ fields can have, if the 3-D coil set-up is not optimised for decoupling edge and core resonances. This component can then couple to the $q = 2$ surface potentially leading to mode locking and consequent substantial confinement degradation or even a disruption

https://doi.org/10.1017/S0022377826101421 Published online by Cambridge University Press

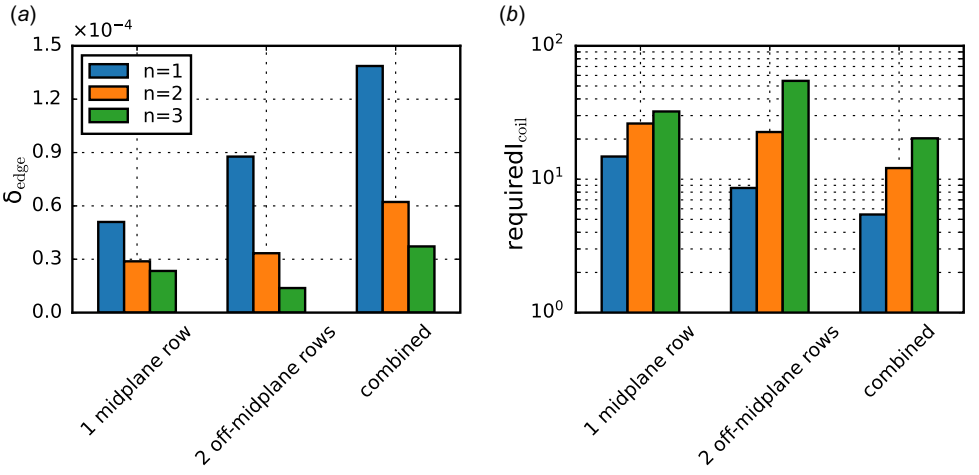


FIGURE 17. Overview of the (*a*) δ_{edge} per kA coil current amplitude, (*b*) required coil current amplitude I_{coil} to meet the RMP ELM suppression criterion of $\delta_{\text{edge}} = 7.5 \times 10^{-4}$.

(Hu *et al*. 2022). With the off-midplane coil set the required currents for ELM suppression with $n = 2$ and $n = 3$ are rather high, but are possible. For the combined coil set of all three rows the current are of the same magnitude as in some of today's experiments.

One crucial issue with RMP ELM suppression is, however, that any of the applied 3-D fields create a very large NTV torque in ARC of several dozens to 100 s of Nm (similar to ITER predictions (Yan *et al*. 2023)). This has the potential to cause strong enough rotational breaking to lead to locked modes and disruptions. If future design changes of ARC make RMP ELM suppression a necessity, more dedicated analysis using quasi-symmetric optimisation of the applied RMP field to minimise the NTV torque (Park *et al*. 2021) may be applied.

6. Conclusions

When designing a future power plant, assessing and mitigating the impact of MHD modes is necessary for high confidence in reliable operation. This work provides a basis for vertical stability control, the ideal kink limit, tearing modes as well as NTMs, and error field correction in the current ARC baseline scenario V3A. Future adjustments to the still evolving ARC design will not only be informed by the presented analysis, but also by insights gathered at SPARC. Applying the same models to assess MHD behaviour in SPARC can serve as validation for the ARC predictions.

Vertical stability control has been shown to be possible using the poloidal shaping coils instead of a dedicated vertical stability coil installed closer to the plasma. This is highly beneficial from an engineering point of view by omitting the need to design, install and maintain vertical stability coils close to the plasma, which is a challenging environment for coils in a high fusion power tokamak. Simulations of vertical displacement events using the MEQ-FGE/FGS/FBT and TokaMaker codes shows that the PF5 coils can be used to control vertical stability with initial displacements of up to 12 cm. This exceeds the widely agreed upon criteria of 5 % of the minor radius, which in case of ARC would be 6 cm. Given this criterion, scans of the power supply

https://doi.org/10.1017/S0022377826101421 Published online by Cambridge University Press

voltage slew rate and vertical control filter delay times can inform the requirements for the power supplies controlling the PF5 coils when the latter are used for vertical stability control. This ranges from a voltage slew rate of approximately 40 kVs^{-1} at a high filter delay time of 500 μs, to 80 kVs^{-1} at 50 μs.

Stability calculations with the DCON code reveal that the ARC baseline scenario operates far away from the beta limit, which is defined by the growth of an external kink mode. Scans of the normalised plasma beta β_N around its nominal value of 1.65 show the ideal kink becoming unstable at $\beta_N = 3.2$ under the most unstable assumption of no wall and no kinetic effects. This is being stabilised further by including a conducting wall as well as kinetic damping. To find the most realistic beta limit from artificial beta scans, TokaMaker was used to create free-boundary equilibria with self-consistent bootstrap current.

The stability of tearing modes is described by a negative classical tearing stability index $\Delta' < 0$. At the $m/n = 3/2$ and $2/1$ rational surfaces of the ARC baseline scenario, Δ' through the whole scanned range of $0.5 < \beta_N < 2.5$ and $0.92 < l_i < 1.15$ is always positive, i.e. tearing modes are linearly unstable, as calculated by RDCON. However, including Glasser stabilisation suggests stability for the range of profiles explored. Yet, other transient instabilities such as sawteeth can still seed magnetic islands which can grow into NTMs, if their width is above the marginally stable island width. The toroidal modified Rutherford equation was used to model the evolution of tearing modes and determine the marginal island width for the $m/n = 3/2$ and $2/1$ modes. In the extreme cases of an ideal wall and low $l_i = 0.93$, the marginally stable island width was calculated to be below 0.1 % of the normalised poloidal flux. This raises major concern as it would suggest that virtually any seeding events have the potential to trigger NTMs. While empirical scalings of the critical β_N for NTM onset as well as expected large sawteeth due to fast ion stabilisation show concerning trends, the scaling of seed islands sizes towards FPPs is more optimistic. However, there is a total lack of experimental data especially at FPP relevant normalised ion Larmor radii. This together with the fact that the stability analysis for classical and NTMs is highly sensitive to the uncertainties in kinetic profiles means that a proper model verification with experimental data and rigorous uncertainty quantification are necessary before drawing ultimate conclusions on the impact of NTMs on ARC and how to address them. This is the subject of significant ongoing effort and will benefit hugely from SPARC data, which bridges the gap from today's tokamaks to an FPP.

The critical $n = 1$ error field leading to a disruption in ARC was predicted by an empirical multi-machine model to be larger than in SPARC but smaller than in ITER. This suggests that the demands to an axisymmetric design, manufacturing and assembly are at the level of current engineering experience. In order to inform a set of EFCCs for $n = 1$ error field correction, wide scans of different error geometries are performed which includes the size and location in the poloidal plane as well as its distance and orientation to the plasma surface. The coupling of the EFCCs to the dominant $n = 1$ eigenmode of the plasma does not show an optimum coil size when the coils are installed outside the TF coil, but bigger is generally better and reduced required coil currents. The scan of poloidal location and orientation relative to the plasma surface show an optimum on the LFS off-midplane with coils parallel to the plasma surface. A simple model can be used to include an approximation of the rotation braking effect by the NTV torque and inform a maximum correctable error field. This limit appears due to the scaling of the NTV torque with the square of the EFCC current while the correction field strength only scales linearly. Using

https://doi.org/10.1017/S0022377826101421 Published online by Cambridge University Press

this metric and the engineering limitation to mount the EFCCs on the TF coils, an optimal coil set has been identified to be on the LFS off-midplane symmetrically above and below the midplane. We assume that finding a solution for EFCCs that has the capability to correct for error fields as high as twice the critical error field for disruptions provides sufficient safety margin. This is achieved with two rows of off-midplane coils with a coil height of 2 m and a total coil current amplitude of less than 20 kA. Because the NTV drive peaks sharply around the LFS midplane, a single row of midplane EFCCs is not suitable for error field correction in ARC. Furthermore, we showed that $n = 2$ error field correction is only possible to a small degree and requires the off-midplane coils. The optimised coil set also couples well enough to the edge dominant mode which according to the current understanding of the scaling of RMP requirements will provide strong enough fields to suppress ELMs with reasonably large, required coil currents. Lastly, this study shows the high sensitivity of the NTV drive, and hence the simple model for error field correction, on the plasma rotation, and rotation predictions for future devices are highly uncertain in the core and have no reasonable physics basis for the edge rotation at all. This highlights the necessity for better predictive models to increase the fidelity of EFCC designs. Since the EFCC set for SPARC has been developed using similar approaches and predictions, it will serve as a validation for the ARC design.

Acknowledgments

This work was funded by Commonwealth Fusion Systems. This material is based upon work supported by the U.S. Department of Energy, Office of Science, Fusion Energy Sciences, under the Milestone-Based Fusion Development Program under Award Number DE-SC0024885. We would also like to thank Dr C. Chrystal for his helpful discussions on plasma rotations.

Editor Troy Carter thanks the referees for their advice in evaluating this article.

Disclaimer

This report was prepared as an account of work sponsored by an agency of the United States Government. Neither the United States Government nor any agency thereof, nor any of their employees, makes any warranty, express or implied, or assumes any legal liability or responsibility for the accuracy, completeness or usefulness of any information, apparatus, product, or process disclosed, or represents that its use would not infringe privately owned rights. Reference herein to any specific commercial product, process or service by trade name, trademark, manufacturer or otherwise does not necessarily constitute or imply its endorsement, recommendation or favouring by the United States Government or any agency thereof. The views and opinions of authors expressed herein do not necessarily state or reflect those of the United States Government or any agency thereof.

Declaration of interests

The authors report no conflicts of interest.

Appendix A. The Generalised Perturbed Equilibrium Code modelling framework

A modelling suite comprising the DCON code (Glasser 2016), the GPEC (Park *et al*. 2007, 2009) and the PENTRC (Park 2011; Logan *et al*. 2013) is used to calculate metrics used for optimising a set of 3-D coils for error field correction. All

https://doi.org/10.1017/S0022377826101421 Published online by Cambridge University Press

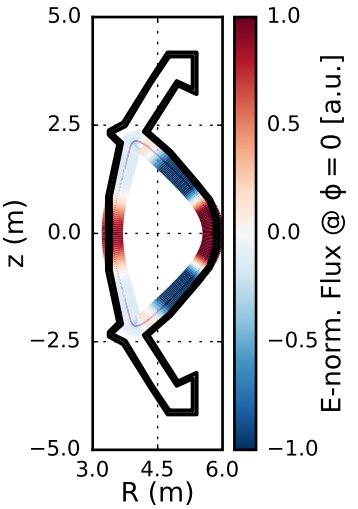


FIGURE 18. Poloidal cross-section illustrating the poloidal mode structure of the core dominant mode projected on the plasma boundary by plotting the energy normalised flux.

these codes utilise a Fourier decomposition of the poloidal and toroidal coordinates in order to describe the non-axisymmetric surface perturbations and perturbations with different toroidal mode numbers n are treated separately in these codes. The workflow is as follows.

The DCON code is used for calculating the ideal or kinetic (requires kinetic profiles) MHD stability for a given axisymmetric equilibrium. It iterates through various edge truncations and identifies the truncation which leads to the most stable equilibrium. This stable, truncated equilibrium is then forwarded to GPEC together with 3-D coil geometries and currents.

Then GPEC calculates the plasma response to the externally applied field. Due to its linear nature, GPEC can utilise a matrix formalism that allows for time efficient post analysis. One such matrix is the resonant coupling matrix $\boldsymbol{C}_{\mathbf{xe}}$, which relates the flux of the externally applied perturbation field Φ_{xe} to the flux on each resonant surfaces $\Phi_{\mathrm{res}} = \boldsymbol{C}_{\mathbf{xe}} \cdot \Phi_{\mathrm{xe}}$. Here, $\boldsymbol{C}_{\mathbf{xe}}$ is a $m \times r$ matrix with m being the number of poloidal modes and r being the number of resonant surfaces in the plasma based on the chosen toroidal mode number and the range of poloidal mode numbers. A singular value decomposition can be performed for $\boldsymbol{C}_{\mathbf{xe}}$, which provides the eigenmodes and associated eigenvalues of the coupling matrix. For typical plasma equilibria and 3-D coils usually one eigenvalue and eigenmode stand out, which is responsible for the largest contribution to the plasma response. This mode is dubbed the dominant mode and its right singular vector is referred to as Φ_{dom}. Figure 18 shows the poloidal cross-section of the dominant eigenmode of the ARC equilibrium projected on the plasma boundary.

Lastly, if DCON and GPEC are ran including kinetic effects, PENTRC can then be used to calculate the NTV torque caused by the perturbation field. The torque matrix $\boldsymbol{T}_{\mathbf{xe}}$, which relates the flux of the externally applied perturbation field Φ_{xe} to the integrated (core to a given flux surface Ψ) torque $T(\Psi) = \Phi_{\mathrm{xe}} \cdot \boldsymbol{T}_{\mathbf{xe}} \cdot \Phi_{\mathrm{xe}}$. Here, $\boldsymbol{T}_{\mathbf{xe}}$ is a $m \times s$ matrix with s being the number of flux surfaces. We refer to the torque across the whole plasma as T_{NTV}.

Using the dominant mode Φ_{dom} and the NTV torque T_{NTV} the following two metrics used for optimising the 3-D coil design can be defined.

https://doi.org/10.1017/S0022377826101421 Published online by Cambridge University Press

Dominant mode overlap δ

The first metric is the dominant mode overlap $\delta = (\Phi_{\mathrm{dom}} \cdot \Phi_{\mathrm{xe}})/B_{\mathrm{T}}$, that is the overlap between the externally applied field and the dominant mode normalised to the toroidal field B_{T}. The externally applied field can be of any nature, i.e. the dominant mode overlap can be used to describe error fields as well as intentionally applied 3-D fields. Throughout this work, when δ is calculated to describe a set of 3-D coils, they are powered such that the coil with the highest current is carrying exactly 1 kA. This way δ can be seen as an efficiency metric describing the coupling strength of the externally applied 3-D field to the plasma per 1 kA coil current.

Furthermore, since the coil coupling matrix C_{xe} describes the coupling to the specific resonant surfaces in its columns, the coupling only to a selected number of resonant surfaces can be achieved by dropping the remaining columns. The safety factor q profile of the ARC equilibrium is shown in figure 2 with the locations of resonant surfaces for toroidal mode numbers of $n = 1, 2, 3$ being marked. When optimising the 3-D coils for error field correction the focus is set on core modes, especially the $m/n = 2/1$ mode as locked modes on that resonant surface are most likely to lead to a disruption. Therefore, δ_{core} is used for optimisation which describes the overlap of the externally applied 3-D field with the dominant mode that drives most core resonance in the region of $\Psi = 0.0$–0.9. As a metric for ELM control, the overlap of the externally applied 3-D field with the dominant mode that drives most edge resonance δ_{edge} is used covering 1–2 resonant surfaces close to the pedestal top.

Maximum correctable error field δ_{max}

The second metric used in this work is the maximum correctable error field δ_{max}. While the first metric δ is an efficiency metric, δ_{max} tries to describe the largest possible error field that can be corrected for given a 3-D coil design. It is based on a simple model that is described in the following including the assumptions going into the model.

At a critical error field δ_{crit} mode locking occurs followed by a disruption. Therefore, the coil current I in the 3-D coils needs to be large enough such that any given error field δ_{EF} balanced by the correction by the 3-D fields $C \cdot I$ is smaller than δ_{crit}

$$\delta_{\mathrm{crit}} > \delta_{\mathrm{EF}} - \boldsymbol{C} \cdot I. \tag{A1}$$

Since the correction term is linear with I this would assume that error fields of any magnitude can be corrected for when I is large enough (see blue linear curve in figure 19). However, it is generally observed that δ_{crit} is smaller the slower a plasma rotates (La Haye *et al*. 1992) and we assume that when the plasma rotation is basically zero an infinitesimal small error field already leads to mode locking. Note that even when error field correction is applied by the 3-D coils, the intrinsic error field can never be completely corrected for due to the geometric limitations of the 3-D coils and the complex structure of error fields. When 3-D fields are applied to a plasma, the NTV torque induced by the toroidal asymmetry brakes the plasma rotation (Shaing & Callen 1983) and we assume zero rotation when the NTV torque balances the intrinsic torque T_0 of the plasma. Including this NTV effect into (A1) leads to the simple model

$$\delta_{\mathrm{crit}} \cdot (T_0 - \boldsymbol{T}_{\mathbf{NTV}} \cdot I^2)/T_0 > \delta_{\mathrm{EF}} - \boldsymbol{C} \cdot I. \tag{A2}$$

Due to that quadratic dependence of the NTV torque on I, this causes the curve in figure 19 to curl back (red line). The model is valid while the total torque

https://doi.org/10.1017/S0022377826101421 Published online by Cambridge University Press

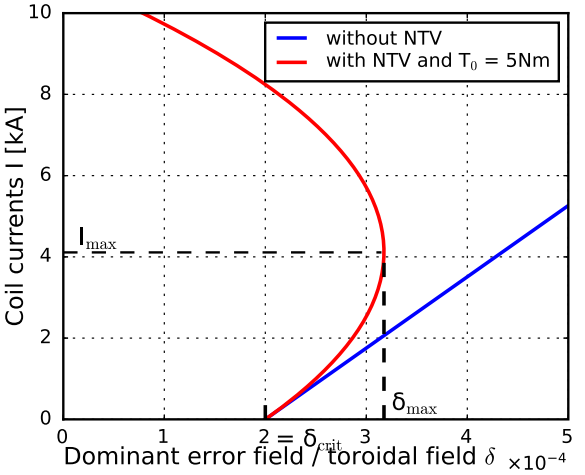


FIGURE 19. Current in the EFCC as a function of the dominant error field normalised by the toroidal field δ. The critical error field δ_{crit} as extrapolated in § 5.1. The case without the NTV torque effect is shown in blue, the case including the NTV torque effect at an intrinsic torque of $T_0 = 5$ Nm is shown in red.

$T_{\mathrm{total}} = T_0 - \boldsymbol{T}_{\mathbf{NTV}} \cdot I^2$ is larger than 0. When $T_{\mathrm{total}} = 0$ we assume that any infinitesimal small error field already leads to mode locking and the error field at which this conditions is fulfilled we call the maximum correctable error field δ_{max} and the corresponding 3-D coil current I_{max}.

REFERENCES

BARDÓCZI, L., DUDKOVSKAIA, A., LOGAN, N., RICHNER, N., BROWN, A., CALLEN, J., LA HAYE, R. & STRAIT, E. 2025 Tearing stable stationary ITER baseline operation in DIII-D. *Nucl. Fusion* **65**, 026049.

BENJAMIN, S., KEITH, Z., MARIS, A., KUMAR, A., LOGAN, N., HANSEN, C., HOWELL, E., MARMAR, E. & REA, C. 2026 Macroscopic trends of neoclassical tearing stability in high-field h-mode tokamak pilot plants. *Nucl. Fusion* **66**, 036049.

BODY, T. 2025 cfspopcon. Available at: https://github.com/cfs-energy/cfspopcon.

BRENNAN, D.P., TURNBULL, A.D., CHU, M.S., LA HAYE, R.J., LAO, L.L., OSBORNE, T.H. & GALKIN, S.A. 2007 Resistive stability of 2/1 modes near 1/1 resonance. *Phys. Plasmas* **14**, 056108.

BUTTERY, R.J., GERHARDT, S., LA HAYE, R.J., LIU, Y.Q., REIMERDES, H., SABBAGH, S., CHU, M.S., OSBORNE, T.H., PARK, J.-K., PINSKER, R.I., STRAIT, E.J., YU, J.H. 2011 The impact of 3D fields on tearing mode stability of H-modes. *Nucl. Fusion* **51**, 073016.

BUTTERY, R., *et al.* 2000 Neoclassical tearing modes. *Plasma Phys. Control. Fusion* **42**, B61–B73.

BUTTERY, R.J., LA HAYE, R.J., GOHIL, P., JACKSON, G.L., REIMERDES, H., STRAIT, E.J. & the DIII-D Team 2008 The influence of rotation on the βN threshold for the 2/1 neoclassical tearing mode in DIII-D. *Phys. Plasmas* **15**, 056115.

CARPANESE, F. 2021 Development of free-boundary equilibrium and transport solvers for simulation and real-time interpretation of tokamak experiments. *Nucl. Fusion* **7914**, 238.

CHRYSTAL, C., GRIERSON, B., HASKEY, S., SONTAG, A., POLI, F., SHAFER, M. & DEGRASSIE, J. 2020 Predicting the rotation profile in iter. *Nucl. Fusion* **60**, 036003.

DUDSON, B. 2024 Freegs. Available at: https://github.com/freegs-plasma/freegs.

EICH, T. *et al*. 2026 Power and particle exhaust for the ARC fusion power plant. *J. Plasma Phys.* **92**, E66. https://doi.org/10.1017/S002237782610155X.

FENSTERMACHER, M., *et al.* 2025 Progress in pedestal and edge physics: Chapter 3 of the special issue: on the path to tokamak burning plasma operation. *Nucl. Fusion* **65**, 053001.

https://doi.org/10.1017/S0022377826101421 Published online by Cambridge University Press

FITZPATRICK, R. 1995 Helical temperature perturbations associated with tearing modes in tokamak plasmas. *Phys. Plasmas* **2**, 825–838.

FITZPATRICK, R. 2023 *Tearing Mode Dynamics in Tokamak Plasmas*, vol. 1, pp. 2053–2563. IOP Publishing.

FITZPATRICK, R. 2025 Investigation of tearing mode stability near ideal stability boundaries via asymptotic matching techniques. arXiv: 2503.24184.

FOUSSAT, A., LIBEYRE, P., MITCHELL, N., GRIBOV, Y., JONG, C., BESSETTE, D., GALLIX, R., BAUER, P. & SAHU, A. 2010 Overview of the ITER correction coils design. *IEEE Trans. Appl. Supercond.* **30**, 402–406.

FURTH, H.P. 1973 Tearing mode in the cylindrical tokamak. *Phys. Fluids* **16**, 1054.

GLASSER, A.H. 2016 The direct criterion of newcomb for the ideal MHD stability of an axisymmetric toroidal plasma. *Phys. Plasmas* **23**, 072505.

GLASSER, A.H., GREENE, J.M. & JOHNSON, J.L. 1975 Resistive instabilities in general toroidal plasma configurations. *Phys. Fluids* **18**, 875–888.

GLASSER, A.S. & KOLEMEN, E. 2018 A robust solution for the resistive mhd toroidal deltaprime matrix in near real-time. *Phys. Plasmas* **25**, 082502.

GRIERSON, B., BURRELL, K., SOLOMON, W., BUDNY, R. & CANDY, J. 2013 Collisionality scaling of main-ion toroidal and poloidal rotation in low torque DIII-D plasmas. *Nucl. Fusion* **53**, 063010.

GUIZZO, S., NELSON, A.O., HANSEN, C., LOGAK, F. & PAZ-SOLDAN, C. 2024 Assessment of vertical stability for negative triangularity pilot plants. *Plasma Phys. Control. Fusion* **66**, 065018.

HAHN, S.-H., *et al.* 2020 Advances and challenges in KSTAR plasma control toward long-pulse, high-performance experiments. *Fusion Eng. Des.* **156**, 111622.

HANSEN, C., STEWART, I., BURGESS, D., PHARR, M., GUIZZO, S., LOGAK, F., NELSON, A.O. & PAZ-SOLDAN, C. 2024 Tokamaker: an open-source time-dependent grad-shafranov tool for the design and modeling of axisymmetric fusion devices. *J. Comput. Phys.* **298**, 109111.

HEGNA, C.C. 1999 Nonlinear dynamics of pressure driven magnetic islands in low aspect ratio tokamaks. *Phys. Plasmas* **6**, 3980–3989.

HENDER, T., HOWELL, D., BUTTERY, R., SAUTER, O., SARTORI, F., HAYE, R.L., HYATT, A., PETTY, C., CONTRIBUTORS, J.E. & the DIII-D team 2024 Comparison of $m = 2$, $n = 1$ neo-classical tearing mode limits in jet and dIII-D. *Nucl. Fusion* **44**, 788.

HILLESHEIM, J., *et al.* 2026 Overview of the physics basis for the ARC fusion power plant. *J. Plasma Phys.* **92**, E69. https://doi.org/10.1017/S0022377826101706.

HOWARD, N., *et al.* 2026 Performance and transport in the ARC tokamak. *J. Plasma Phys.* **92**, E67. https://doi.org/10.1017/S0022377826101573.

HU, Q., DU, X., YU, Q., LOGAN, N., KOLEMEN, E., NAZIKIAN, R. & JIANG, Z. 2022 Fast and pervasive heat transport induced by multiple locked modes in DIII-D. *Nucl. Fusion* **59**, 016005.

HU, Q.M., NAZIKIAN, R., GRIERSON, B.A., LOGAN, N.C., ORLOV, D.M., PAZ-SOLDAN, C. & YU, Q. 2020 Wide operational windows of edge-localized mode suppression by resonant magnetic perturbations in the DIII-D tokamak. *Phys. Rev. Lett.* **125**, 045001.

HUMPHREYS, D.A. *et al.* 2009 Experimental vertical stability studies for ITER performance and design guidance. *Nucl. Fusion* **49**, 115003.

ISHIZAWA, A., WAELBROECK, F.L., FITZPATRICK, R., HORTON, W. & NAKAJIMA, N. 2012 Magnetic island evolution in hot ion plasmas. *Phys. Plasmas* **19**, 072312.

JANZ, G. 1988 Thermodynamic and transport properties for molten salts: correlation equations for critically evaluated density, surface tension, electrical conductance, and viscosity data. *J. Phys. Chem. Refer. Data* **17**, 175.

KIM, K., PARK, J.M., LA HAYE, R.J. & NA, Y.-S. 2025 Integrated modeling of advanced tokamaks for tearing mode avoidance on dIII-D. *Phys. Plasmas* **32**, 022510.

KOTSCHENREUTHER, M., HAZELTINE, R.D. & MORRISON, P.J. 1985 Nonlinear dynamics of magnetic islands with curvature and pressure. *Phys. Fluids* **28**, 294–302.

KUMAR, A., CLAUSER, C., CARPANESE, F., WAI, J., GOLFINOPOULOS, T., BATTAGLIA, D., GARNIER, D., GRANETZ, R., SWEENEY, R. & BOYER, D. 2026 Vertical growth rate modeling in alcator c-mod and sparc: rigid vs. non-rigid body approaches. *Plasma Phys. Control. Fusion* (accepted). https://doi.org/10.1088/1361-6587/ae4715

https://doi.org/10.1017/S0022377826101421 Published online by Cambridge University Press

La Haye, R., Chrystal, C., Strait, E., Callen, J., Hegna, C., Howell, E., Okabayashi, M. & Wilcox, R. 2022 Disruptive neoclassical tearing mode seeding in DIII-D with implications for ITER. *Nucl. Fusion* **62**, 056017.

La Haye, R., Petty, C., Politzer, P. & the DIII-D Team 2011 Influence of plasma flow shear on tearing in DIII-D hybrids. *Nucl. Fusion* **51**, 053013.

La Haye, R.J. 2006 Neoclassical tearing modes and their control. *Phys. Plasmas* **13**, 055501.

La Haye, R.J. 2017 Forecasting electron cyclotron current drive stabilization of neoclassical tearing modes in ITER. *EPJ Web Conf.* **157**, 03027.

La Haye, R.J., Brennan, D.P., Buttery, R.J. & Gerhardt, S.P. 2010 Islands in the stream: the effect of plasma flow on tearing stabilitya. *Phys. Plasmas* **17**, 056110.

La Haye, R.J. & Buttery, R.J. 2009 The stabilizing effect of flow shear on m/n=3/2 magnetic island width in dIII-D. *Phys. Plasmas* **16**, 022107.

La Haye, R.J., Buttery, R.J., Günter, S., Huysmans, G.T.A., Maraschek, M. & Wilson, H.R. 2000 Dimensionless scaling of the critical beta for onset of a neoclassical tearing mode. *Phys. Plasmas* **7**, 3349–3359.

La Haye, R.J., Fitzpatrick, R., Hender, T.C., Morris, A.W., Scoville, J.T. & Todd, T.N. 1992 Critical error fields for locked mode instability in tokamaks. *Phys. Fluids B: Plasma Phys.* **4**, 2098–2103.

Logan, N. *et al.* 2025 Metrics and extrapolation of resonant magnetic perturbation thresholds for ELM suppression. *Nucl. Fusion* **65**, 076029.

Logan, N. *et al.* 2020 Empirical scaling of the $n = 2$ error field penetration threshold in tokamaks. *Nucl. Fusion* **60**, 086010.

Logan, N., Paz-Soldan, C., Creely, A. & Sweeney, R. 2022 Sparc 3d field physics and support of the non-axisymmetric coil assessment. *Tech. Rep.* LLNL-SR-832867; 1047216. Lawrence Livermore National Laboratory (LLNL). Available at: https://www.osti.gov/biblio/1860838.

Logan, N.C., Park, J.-K., Kim, K., Wang, Z. & Berkery, J.W. 2013 Neoclassical toroidal viscosity in perturbed equilibria with general tokamak geometry. *Phys. Plasmas* **20**, 122507.

Lütjens, H., Luciani, J.-F. & Garbet, X. 2001 Curvature effects on the dynamics of tearing modes in tokamaks. *Phys. Plasmas* **8**, 4267–4270.

Nelson, A.O., Garnier, D.T., Battaglia, D., Paz-Soldan, C., Stewart, I., Reinke, M., Creely, A. & Wai, J. 2024 Implications of vertical stability control on the SPARC tokamak. *Nucl. Fusion* **64**, 086040.

Nelson, A.O., Hyatt, A.W., Wehner, W.P., Welander, A.S., Paz-Soldan, C., Osborne, T.H., Anand, H. & Thome, K.E. 2023 Vertical control of DIII-d discharges with strong negative triangularity. *Plasma Phys. Control. Fusion* **65**, 044002.

Newcomb, W.A. 1960 The direct criterion of newcomb for the ideal MHD stability of an axisymmetric toroidal plasma. *Ann. Phys.* **10**, 232–267.

Park, J.-K. 2011 Kinetic energy principle and neoclassical toroidal torque in tokamaks. *Phys. Plasmas* **18**, 110702.

Park, J.-K., Boozer, A., Menard, J., Garofalo, A., Schaffer, M., Hawryluk, R., Kaye, S., Gerhardt, S., Sabbagh, S. & Team, N.S.T.X. 2009 Importance of plasma response to nonaxisymmetric perturbations in tokamaks. *Phys. Plasmas* **16**, 056115.

Park, J.-K., Boozer, A.H. & Glasser, A.H. 2007 Computation of three-dimensional tokamak and spherical torus equilibria. *Phys. Plasmas* **14**, 052110.

Park, J.-K. & Logan, N. 2017 Self-consistent perturbed equilibrium with neoclassical toroidal torque in tokamaks. *Phys. Plasmas* **24**, 032505.

Park, J.-K., Yang, S., Logan, N., Hu, Q., Zhu, C., Zarnstorff, M., Nazikian, R., Paz-Soldan, C., Jeon, Y. & Ko, W. 2021 Quasisymmetric optimization of nonaxisymmetry in tokamaks. *Phys. Rev. Lett.* **126**, 125001.

Pereverzev, G.V. & Yushmanov, P.N. 1991 ASTRA: automated system for transport analysis. *Tech. Rep.* IPP–5/42. Max-Planck-Institut for Plasma Physics. Available at: https://inis.iaea.org/records/gqajm-8zx44.

Pucella, G. *et al.* 2021 Onset of tearing modes in plasma termination on JET: the role of temperature hollowing and edge cooling. *Nucl. Fusion* **61**, 046020.

https://doi.org/10.1017/S0022377826101421 Published online by Cambridge University Press

RICE, J., CAO, N., TALA, T., CHRYSTAL, C., GREENWALD, M., HUGHES, J., MARMAR, E., REINKE, M., FERNANDEZ, P.R. & SALMI, A. 2021 Dimensionless parameter scaling of intrinsic torque in C-Mod enhanced confinement plasmas. *Nucl. Fusion* **61**, 026013.

RICE, J., *et al.* 2007 Inter-machine comparison of intrinsic toroidal rotation in tokamaks. *Nucl. Fusion* **47**, 1618–1624.

RUTHERFORD, P.H. 1973 Nonlinear growth of the tearing mode. *Phys. Fluids* **16**, 1903.

SAUTER, O., ANGIONI, C. & LIN-LIU, Y. 1999 Neoclassical conductivity and bootstrap current formulas for general axisymmetric equilibria and arbitrary collisionality regime. *Phys. Plasmas* **6**, 2834–2839.

SCHLUTT, M.G. & HEGNA, C.C. 2012 The effect of anisotropic heat transport on magnetic islands in 3-D configurations. *Phys. Plasmas* **19**, 082514.

SHAING, K. & CALLEN, J. 1983 Neoclassical flows and transport in nonaxisymmetric toroidal plasmas. *Phys. Fluids* **26**, 3315–3326.

SNYDER, P., GROEBNER, R., HUGHES, J., OSBORNE, T., BEURSKENS, M., LEONARD, A., WILSON, H. & XU, X. 2011 A first-principles predictive model of the pedestal height and width: development, testing and iter optimization with the eped model. *Nucl. Fusion* **51**, 103016.

SNYDER, P., OSBORNE, T., BURRELL, K., GROEBNER, R., LEONARD, A., NAZIKIAN, R., ORLOV, D., SCHMITZ, O., WADE, M. & WILSON, H. 2012 The EPED pedestal model and edge localized mode-suppressed regimes: studies of quiescent H-mode and development of a model for edge localized mode suppression via resonant magnetic perturbations. *Phys. Plasmas* **19**, 056115.

SNYDER, P.B., GROEBNER, R.J., LEONARD, A.W., OSBORNE, T. & WILSON, H.R. 2009 Development and validation of a predictive model for the pedestal height. *Phys. Plasmas* **16**, 056118.

STAEBLER, G.M., CANDY, J., BELLI, E.A., KINSEY, J.E., BONANOMI, N. & PATEL, B. 2020 Geometry dependence of the fluctuation intensity in gyrokinetic turbulence. *Plasma Phys. Control. Fusion* **63**, 015013.

STAEBLER, G.M., KINSEY, J.E. & WALTZ, R.E. 2004 A theory-based transport model with comprehensive physics. *Phys. Plasmas* **14**, 055909.

STRAIT, E. 2005 Stability limits of high-beta plasmas in dIII-D. *Fusion Sci. Technol.* **48** (2), 864–874.

SWEENEY, R., *et al.* 2026 ARC disruption physics and strategy. *J. Plasma Phys.* **92**, E68. https://doi.org/10.1017/S0022377826101585.

SWEENEY, R., CHOI, W., LA HAYE, R., MAO, S., OLOFSSON, K. & VOLPE, F. 2017 Statistical analysis of $m/n = 2/1$ locked and quasi-stationary modes with rotating precursors at DIII-D. *Nucl. Fusion* **57** (1), 016019.

VIEZZER, E., PÜTTERICH, T., ANGIONI, C., BERGMANN, A., DUX, R., FABLE, E., MCDERMOTT, R.M., STROTH, U., WOLFRUM, E., the ASDEX Upgrade Team 2013 Evidence for the neoclassical nature of the radial electric field in the edge transport barrier of asdex upgrade. *Nucl. Fusion* **54** (1), 012003.

VILLONE, F., BARBATO, L., MASTROSTEFANO, S. & VENTRE, S. 2013 Coupling of nonlinear axisymmetric plasma evolution with three-dimensional volumetric conductors. *Plasma Phys. Control. Fusion* **55** (9), 095008.

DE VRIES, P., JOHNSON, M., ALPER, B., BURATTI, P., HENDER, T., KOSLOWSKI, H., RICCARDO, V. & CONTRIBUTORS, J.-E. 2011 Survey of disruption causes at jet. *Nucl. Fusion* **51** (5), 053018.

WAELBROECK, F.L. 2005 Natural velocity of magnetic islands. *Phys. Rev. Lett.* **95** (3), 035002.

YAN, X.-T., SUN, Y.-W., LI, L., LIU, Y.-Q., BAO, N.-N., LOARTE, A., PINCHES, S. & WAN, B.-N. 2023 Modeling of toroidal momentum transport induced by neoclassical toroidal viscosity torque for iter scenarios. *Nucl. Fusion* **63** (9), 096020.

YU, Q., GÜNTER, S., LACKNER, K., STRUMBERGER, E. & IGOCHINE, V. 2019 Numerical study on toroidal mode coupling and triggering of neoclassical tearing modes by sawteeth. *Nucl. Fusion* **59**, 106053.

ZIMMERMANN, C. *et al.* 2024 Experimental validation of momentum transport theory in the core of H-mode plasmas in the ASDEX Upgrade tokamak. *Phys. Plasmas* **31**, 042306.

https://doi.org/10.1017/S0022377826101421 Published online by Cambridge University Press